# Large-scale shell-model calculations of elastic and inelastic scattering rates of lightest supersymmetric particles (LSP) on $^{127}$I, $^{129}$Xe, $^{131}$Xe, and $^{133}$Cs nuclei

P. Toivanen, M. Kortelainen, J. Suhonen, and J. Toivanen
*Department of Physics, University of Jyväskylä, Post Office Box 35, FIN-40014 Jyväskylä, Finland*
(Received 27 October 2008; published 2 April 2009)

We discuss the dark-matter detection rates for the elastic and inelastic scattering of the lightest supersymmetric particle (LSP) off nuclei. For this we use an easily accessible formalism where the underlying nuclear physics is condensed in structure coefficients multiplying the key parameters of supersymmetric theories. In this work we compute these coefficients for the stable iodine, xenon, and cesium nuclei by application of the nuclear shell model in a model space involving the $2s$, $1d$, $0g_{7/2}$, and $0h_{11/2}$ single-particle orbitals. As an interaction we use the renormalized Bonn-CD $G$ matrix. By using fitted nuclear gyromagnetic factors we have successfully reproduced the relevant spectroscopic data on magnetic moments and $M1$ decays in the discussed nuclei.

DOI: 10.1103/PhysRevC.79.044302 PACS number(s): 21.60.Cs, 23.40.Hc, 27.60.+j

## I. INTRODUCTION

According to present conception an overwhelming part of the energy content of the Universe is made up of dark energy and dark matter. The dark-matter component exhausts some 30% of the energy balance and is mostly in the form of cold dark matter (CDM). The CDM is believed to consist of nonrelativistic heavy particles called WIMPs (weakly interacting massive particles). The first observational indications of the existence of dark matter were the rotational curves of galaxies [1]. The WIMPs are believed to constitute the major component of dark matter in our own galactic halo.

WIMPs interact very weakly with ordinary matter, which makes them extremely difficult to detect. For the moment, the only way to access the nature of dark matter is by direct detection experiments in laboratories. These experiments look for recoil signals of the nucleus on which the WIMP has scattered elastically or inelastically. The average nuclear recoil energies in WIMP-nucleus scattering are typically less than few tens of keV and thus very sensitive detectors with low energy thresholds are needed. Furthermore, the interaction rate in WIMP-nucleus scattering is very low (less than one event/kg/yr according to present experimental evidence) so that the cosmic rays and other background become a serious problem. Because of these complications the experiments are located in underground facilities and protected with extensive shielding.

At the moment, there are a great number of different experiments to detect WIMPs. For example, for light WIMP masses an ultra-low-energy germanium detector has been developed by the TEXONO Collaboration [2]. For the higher WIMP masses the CDMS [3] and EDELWEISS [4] experiments use germanium crystal detectors. The CRESST experiment [5] uses detectors based on scintillating $CaWO_4$ crystals. Further experiments include the ZEPLIN and XENON experimental programs, with published results for the ZEPLIN I [6] and XENON10 [7] experiments. These experiments use liquid xenon detectors. The liquid xenon detector is also used in the DAMA/WIMP-$^{129}$Xe inelastic scattering experiment [8–10], where the background can be reduced by coincidence signals coming from the de-excitation $\gamma$ rays of the two lowest excited states of $^{129}$Xe. The calculations of the present article are relevant for the DAMA/$^{129}$Xe experiment and also the ZEPLIN and XENON experimental programs since they use $^{129}$Xe and $^{131}$Xe as stable detector materials. Related to this, the planned XMASS 800-kg detector uses ultra-pure liquid xenon and has recently completed a prototype research and development stage [11].

The KIMS experiment has recently reported new limits on the WIMP-nucleon cross section with CsI(Tl) crystal detectors using 3409 kg day exposure data [12]. It is notable that this experiment uses the $^{127}$I and $^{133}$Cs detector nuclei, $^{127}$I being shared with the DAMA experiment discussed in the following, and both nuclei being the topic of study in this paper. The nucleus $^{127}$I is involved also by the NAIAD [13] experiment. Many other experiments have been devised and have taken and/or are currently taking data; these include the ROSEBUD [14] (Al and O as detector nuclei), the SIMPLE [15] ($^{19}$F as detector nucleus), and the PICASSO [16] (again $^{19}$F as detector nucleus) experiments. The recent results of the COUPP experiment [17] are connected with the present article via $^{127}$I, which is one component in the $CF_3I$ target material.

An important characteristic of WIMP-nucleus scattering is its annual modulation. The event rate depends on the direction of the Earth's orbital motion relative to Sun's movement through the Milky Way galactic disk and its dark-matter halo. This modulation can be used to distinguish the WIMP signal from the background. So far the only experiment to measure this modulation is the DAMA/NaI experiment [18–20] that uses scintillating NaI crystals containing the nucleus $^{127}$I, discussed in the present paper. The data of DAMA apparently contradict results of the other experiments, and only a small window is left where the DAMA data could coexist with the other data [12]. In Ref. [21] an attempt was made to reconcile the different observations by the competition of the spin-independent and spin-dependent channels assuming a suitable SUSY scenario for the LSP (lightest supersymmetric particle) dark-matter candidate.

Supersymmetry naturally provides WIMP constituents of the CDM [1]. Here we assume that the WIMP is an LSP. In the minimal supersymmetric standard model (MSSM) the

 

LSP is stable or almost stable and can be simply described as a Majorana fermion that can be formed as the lowest energy linear combination of the neutral components of gauginos and higgsinos [22,23]. The relative weight of different components in the LSP state produces different effects (e.g., in the relic abundance of the LSPs [24]). The LSP scatters off the nuclei via the neutral current interactions, exchanging, for example. a Z boson or a squark [25].

In this work we study both the elastic and inelastic channels of the LSP-nucleus scattering off the $^{127}$I, $^{129}$Xe, $^{131}$Xe, and $^{133}$Cs detector nuclei. We calculate the corresponding detection rates in a SUSY-model-independent way by using nuclear-structure coefficients that separate from the SUSY parameters. For the nuclear-structure calculations we use the nuclear shell model in the full $2s1d0g_{7/2}0h_{11/2}$ valence space for protons and in the $0g_{7/2}1d_{5/2}$-$2s_{1/2}1d_{3/2}0h_{11/2}$ particle-hole space for neutrons. As the two-body interaction we use the renormalized Bonn-CD $G$ matrix. This work is an extension of Ref. [26], where the elastic and inelastic detection rates of the LSP-nucleus scattering off the $^{129}$Xe and $^{131}$Xe nuclei were discussed.

There are few earlier calculations of the elastic LSP-nucleus scattering cross sections available for the nuclei of interest in this paper. In Ref. [27] the independent single-particle shell model and in Ref. [28] the odd group model were applied to a large number of nuclei. In Ref. [29] a very rudimentary nuclear wave function for the ground state of $^{131}$Xe was used to compute the structure functions related to elastic LSP-$^{131}$Xe scattering. In Ref. [30] the interacting boson fermion model (IBFM) was used and in Ref. [31] the theory of finite Fermi systems was applied to several nuclei, including the ones that are under discussion in this work. Later, the elastic LSP-nucleus scattering differential cross sections of the $^{127}$I, $^{129}$Xe, and $^{131}$Xe nuclei were discussed in Ref. [32] by the use of a large-scale shell model with Bonn and Nijmegen-II two-nucleon interactions. In Ref. [32] the adopted single-particle valence space was the same as in this work but the truncations in the number of included configurations were more severe. In Ref. [21] the nucleus $^{127}$I, among others, was studied by computing the elastic LSP-nucleus detection rates in the $2s1d0g_{7/2}0h_{11/2}$ valence space. There the shell-model results were compared with those calculated by the use of the microscopic quasiparticle-phonon model (MQPM) [33].

Only very few earlier works exist for the inelastic channel. In Refs. [34–36] very rough estimates were given for the scattering cross sections or event rates. In none of these works were the needed nuclear wave functions actually calculated in a reliable microscopic nuclear framework. In Ref. [35] the inelastic LSP-nucleus matrix elements were related to $M1$ transition matrix elements between the involved states. As discussed later in this article, our microscopic calculations show that this is not a good approximation in all cases. The first work to address both the elastic and inelastic event rates within a unified and complete nuclear scheme was Ref. [26]. In Ref. [26] event rates for the detector nuclei $^{129}$Xe and $^{131}$Xe were discussed.

This article is organized as follows. In Sec. II we discuss the underlying shell-model calculations for the $^{127}$I, $^{129}$Xe, $^{131}$Xe, and $^{133}$Cs detector nuclei. We discuss our results for the elastic LSP-nucleus scattering rates in Sec. III and those for inelastic scattering in Sec. IV. In Sec. V we discuss the annual modulation effect and apply our formalism to a number of proposed sets of SUSY parameters. In Sec. VI we draw our conclusions.

## II. NUCLEAR-STRUCTURE CALCULATIONS

In the present work we perform large-scale shell-model (SM) calculations in a realistic model space with realistic effective two-body interactions. Details of the calculations are described in the following.

### A. Valence space and truncations

The SM calculations for the nuclei considered here were made using the shell-model code EICODE [37]. The single-particle orbitals $0g_{7/2}$, $1d_{5/2}$, $2s_{1/2}$, $1d_{3/2}$, and $0h_{11/2}$ were used for the nuclei $^{127}$I, $^{129}$Xe, $^{131}$Xe, and $^{133}$Cs of interest in this work. For the nucleon-nucleon two-body interaction we used an effective interaction based on the Bonn-CD $G$ matrix [38]. The starting point of the calculations are the experimental single-particle energies $\varepsilon_{0g_{7/2}} = -0.3$ MeV, $\varepsilon_{1d_{5/2}} = 0.0$, $\varepsilon_{2s_{1/2}} = 1.3$ MeV, $\varepsilon_{1d_{3/2}} = 1.5$ MeV, and $\varepsilon_{0h_{11/2}} = 1.9$ MeV relative to the $Z = 50$ core, as given in the work of Ref. [38]. During the many-body calculation these energies were renormalized by the two-body interactions to produce effective neutron single-particle energies relative to the $N = 64$ core.

The SM calculations for all the nuclei were made using truncated many-body bases. Proton many-body configurations were not restricted because of the small number of valence protons in the calculations. Thus for protons we used the full $2s1d0g_{7/2}0h_{11/2}$ valence space. For neutrons we used the $0g_{7/2}1d_{5/2}$-$2s_{1/2}1d_{3/2}0h_{11/2}$ particle-hole space such that in the case of $^{127}$I and $^{129}$Xe the neutron configurations were restricted to allow at most one-particle-one-hole (1p-1h) excitations from the full $1d_{5/2}$ and $0g_{7/2}$ shells. For $^{129}$Xe the allowed neutron configurations were additionally restricted by their centroid energies using the method of Horoi *et al.* [39]. For the nucleus $^{131}$Xe, up to two-particle-two-hole excitations from the full $1d_{5/2}$ and $0g_{7/2}$ shells were allowed, on top of which also energy-centroid restrictions were imposed. For the nucleus $^{133}$Cs the full neutron $2s1d0g_{7/2}0h_{11/2}$ valence space was used and only the number of configurations was restricted by their centroid energies. The maximum allowed centroid energy relative to the lowest one was 4.0 MeV for $^{129}$Xe, $^{131}$Xe, and $^{133}$Cs.

The resulting energy spectra for the nuclei of interest are compared with experimental data in Figs. 1 and 2. As seen in Fig. 1 the low-energy spectrum of $^{129}$Xe is rather well reproduced by the SM calculation. However, for $^{131}$Xe the calculated lowest $1/2^+$ and $3/2^+$ states are a good 100 keV too high, above the $9/2^-$ and $11/2^-$ states that come too low in energy in the calculations. Here it is worth noting that the lowest $1/2^+$ and $3/2^+$ states that are relevant for elastic and inelastic LSP scattering are grouped next to each other both in the calculations and in experiment.

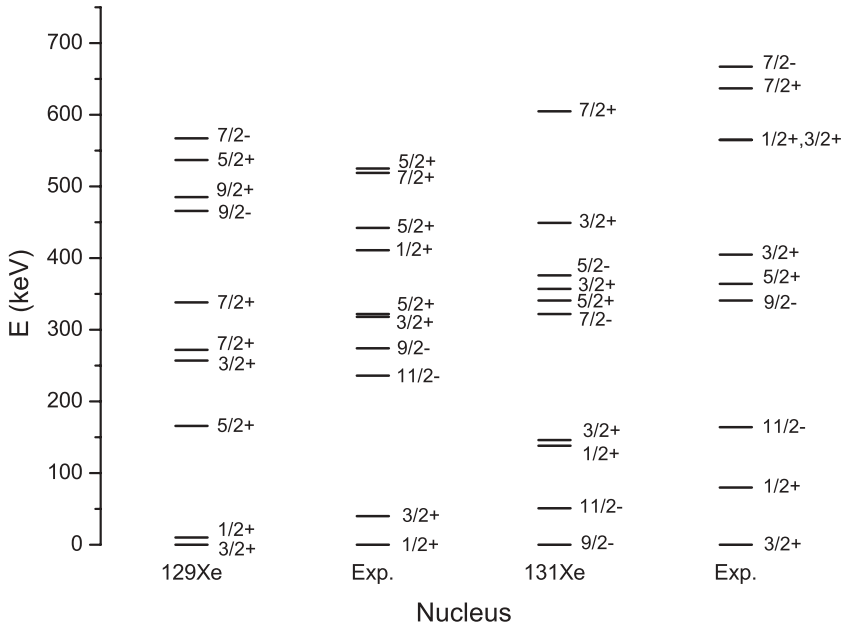


FIG. 1. Comparison of the calculated and experimental energy spectra of $^{129}$Xe and $^{131}$Xe.

In the case of $^{127}$I of Fig. 2 the computed and experimental spectra correspond nicely to each other. The ground state $5/2^+$ is correctly predicted by the SM and the lowest $7/2^+$ state, relevant for inelastic LSP-nucleus scattering, is not far in the computed and experimental spectra. For $^{133}$Cs the situation is not as good, as witnessed from the two rightmost spectra of Fig. 2. The location of the first $5/2^+$ state is almost correctly predicted by the SM but the experimental ground state, $7/2^+$, is predicted some 350 keV too high.

The quality of the wave functions of the first $1/2^+$ and $3/2^+$ states ($^{129}$Xe and $^{131}$Xe) and the first $5/2^+$ and $7/2^+$ states ($^{127}$I and $^{133}$Cs), involved in the LSP-nucleus scattering calculations, can be further tested by computing their magnetic dipole moments and $M1$ decay rates and comparing these with the available data. This is done in the following.

### B. Effective gyromagnetic factors and spin-operator renormalization

When a SM calculation is made in a restricted valence space, such as in a one-oscillator major shell, the renormalized effective interaction must be used to take into account correlation effects coming from outside the model space. This is routinely accomplished in an approximate way by using effective two-body interactions. To be consistent, all other

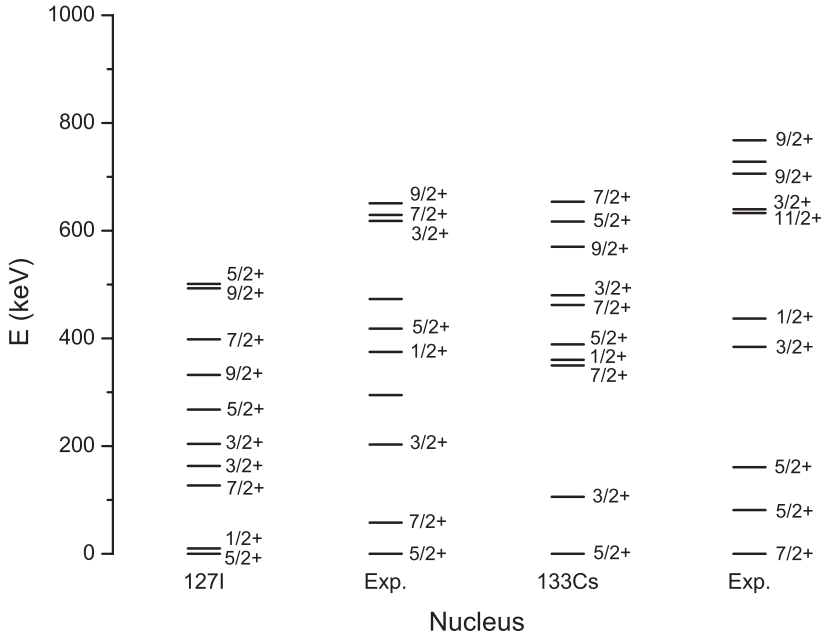


FIG. 2. Comparison of the calculated and experimental energy spectra of $^{127}$I and $^{133}$Cs.

operators should be renormalized too. However, usually other operators, such as electromagnetic multipole operators, are not renormalized. In general, an effective electromagnetic multipole operator has one-body and two-body parts in a two-body cluster approximation and its two-body part is much more complex than its one-body part. Therefore, rigorous renormalization is usually considered too complex and simple approximations for it are used instead.

In the context of the LSP-nucleus scattering the operators of interest are the proton and neutron spin operators and the related magnetic dipole operator. We have looked for a simple renormalization of the magnetic dipole operator by introducing effective spin and orbital angular momentum gyromagnetic factors ($g$ factors). The four optimal effective $g$ factors were determined by a linear least-squares (LLS) fit to 11 known magnetic moments of the nuclei $^{127}$I, $^{129}$Xe, $^{131}$Xe, and $^{133}$Cs. We did not introduce $M1$ transitions to the fit because the phases of the experimental $M1$ matrix elements are unknown. The experimental states used in the fit and their magnetic moments are summarized in Table I. For comparison we have included the Bonn-A results of Ref. [32].

For the xenon isotopes (see Fig. 1) the lowest $1/2^+$, $3/2^+$, and $11/2^-$ states have simple one-particle structure and for each of them a SM state could be assigned without ambiguity. Here one-particle structure means that the dominant component of the shell-model wave function corresponds to a configuration where an odd nucleon occupies the given single-particle state and the rest of the nucleons are paired off to angular momentum zero. Hence, the major component of the wave function corresponds to a seniority-one configuration.

Five magnetic moments are known for these nuclei and all were included in the LLS fit. As discussed earlier, for $^{127}$I and $^{133}$Cs the SM calculations were not able to produce the correct order of energies for their lowest states (see Fig. 2). For $^{127}$I the SM calculations produce the correct $5/2^+$ ground state, but the first excited state is a $1/2^+$ state at 15 keV and the lowest $7/2^+$ state is at 120 keV. The SM also gives two $3/2^+$ states roughly at the energy of the experimentally observed lowest $3/2^+$ state. For the LLS fit we chose the lowest state of each angular momentum and parity for which a magnetic moment is known. In the nucleus $^{133}$Cs magnetic moments are known for the ground state and two lowest $5/2^+$ states. Here we used the corresponding SM states for the LLS fit, even though the SM is not able to produce the correct ground-state angular momentum.

TABLE I. Experimental and calculated magnetic moments in units of $\mu_N/c$. The column "Bare" shows magnetic moments calculated using the standard $g$ factors $g_{s,n} = -3.826$, $g_{s,p} = 5.586$, $g_{l,n} = 0$, and $g_{l,p} = 1$ in units of $\mu_N$. The column "Fitted" shows magnetic moments calculated using effective $g$ factors resulting from the LLS fit. For comparison we have included the Bonn-A results of Ref. [32].

| State | Exp. | Present | | Ref. [32] | |
|---|---|---|---|---|---|
| | | Fitted | Bare | Fitted | Bare |
| $^{127}$I($5/2^+_{g.s.}$) | 2.81 | 2.74 | 3.55 | 2.47 | 2.77 |
| $^{127}$I($3/2^+_1$) | 0.97 | 0.66 | −0.29 | – | – |
| $^{127}$I($7/2^+_1$) | 2.54 | 2.24 | 1.05 | – | – |
| $^{129}$Xe($1/2^+_{g.s.}$) | −0.78 | −0.80 | −0.94 | −0.63 | −0.98 |
| $^{129}$Xe($3/2^+_1$) | 0.58 | 0.47 | 0.45 | – | – |
| $^{129}$Xe($11/2^-_1$) | −0.89 | −0.81 | −1.17 | – | – |
| $^{131}$Xe($3/2^+_{g.s.}$) | 0.69 | 0.68 | 0.72 | 0.64 | 0.98 |
| $^{131}$Xe($11/2^-_1$) | −0.99 | −1.01 | −1.37 | – | – |
| $^{133}$Cs($7/2^+_{g.s.}$) | 2.58 | 2.87 | 1.67 | – | – |
| $^{133}$Cs($5/2^+_1$) | 3.45 | 3.33 | 4.03 | – | – |
| $^{133}$Cs($5/2^+_2$) | 2.00 | 2.31 | 1.82 | – | – |

The $g$ factors resulting from the LLS fit are $g_{s,n} = -3.370$, $g_{s,p} = 3.189$, $g_{l,n} = 0.01903$, and $g_{l,p} = 1.119$ in units of $\mu_N$. The largest renormalization happens for $g_{s,p}$, all other factors being renormalized only by about 10% or less. From Table I one can see that the largest improvements for magnetic moments happen in the proton-odd nuclei $^{127}$I and $^{133}$Cs. This explains the large renormalization of $g_{s,p}$, since for proton-odd nuclei $g_{s,n}$ and $g_{l,n}$ affect the magnetic moments very little (and vice versa for neutron-odd nuclei). The rms error of the LLS fit is $0.2396\mu_N$ compared to an rms error of $0.9117\mu_N$ when using the bare $g$ factors. The use of the fitted effective $g$ factors therefore improves the calculated magnetic moments substantially both for the ground states and for the lowest excited states of the nuclei considered.

The last two columns of Table I list values of magnetic moments coming from the SM calculation of Ref. [32] by using the Bonn-A interaction. The Nijmegen-II calculated results of Ref. [32] are of the same quality as the Bonn-A results and are not included in the table. As can be seen, our fitted magnetic moments are much better than the corresponding ones of Ref. [32]. This is even more striking upon remembering that we have included in our fit also a host of magnetic moments of excited states in the four discussed nuclei, whereas in Ref. [32] only the ground states of $^{125}$Te, $^{127}$I, $^{129}$Xe, and $^{131}$Xe were included.

Table II shows our calculated $B(M1)$ values for the $M1$ decays determined by using either the bare or the effective $g$ factors. The use of effective $g$ factors improves slightly the $M1$ transitions to ground states. The rms deviation of $B(M1)$ values from experimental ones is $0.0376\mu_N/c$ when using the effective operator whereas with the bare operator it is $0.0432\mu_N/c$. We can thus say that the improvement for the ground-state transitions is not significant. The rms deviations are average quantities, and for some states the agreement with experiment actually becomes slightly worse by using the effective $M1$ operator. For transitions between excited states the use of effective $g$ factors improves the calculated results more significantly. Using the effective $g$ factors seems to produce more cancellation between various components of transition matrix elements. This can be seen from the fact that transitions whose experimental $B(M1)$ values are very small are usually reproduced better by the use of the renormalized $M1$ operator.

In conclusion, the renormalization of the $M1$ transition operator substantially improves the description of magnetic moments and also slightly improves the description of $M1$ transitions (on average) when the $g$ factors are determined

TABLE II. $B(M1)$ values for $M1$ transitions between lowest excited states and ground state of the calculated nuclei in units of $(\mu_N/c)^2$. The column "fitted" shows $B(M1)$ values calculated using effective $g$ factors resulting from the LLS fit.

| $M1$ transition | Exp. | Th. (fitted) | Th. (bare) |
|---|---|---|---|
| $^{127}\mathrm{I}(7/2_1^+ \to 5/2_{\mathrm{g.s.}}^+)$ | 0.022 | $8.46 \times 10^{-4}$ | $5.01 \times 10^{-3}$ |
| $^{127}\mathrm{I}(3/2_1^+ \to 5/2_{\mathrm{g.s.}}^+)$ | 0.008 | 0.066 | 0.128 |
| $^{127}\mathrm{I}(5/2_2^+ \to 5/2_{\mathrm{g.s.}}^+)$ | 0.132 | 0.036 | 0.077 |
| $^{129}\mathrm{Xe}(3/2_1^+ \to 1/2_{\mathrm{g.s.}}^+)$ | 0.049 | 0.033 | 0.042 |
| $^{129}\mathrm{Xe}(3/2_2^+ \to 1/2_{\mathrm{g.s.}}^+)$ | $9.85 \times 10^{-3}$ | $1.40 \times 10^{-3}$ | $1.20 \times 10^{-3}$ |
| $^{131}\mathrm{Xe}(1/2_1^+ \to 3/2_{\mathrm{g.s.}}^+)$ | 0.062 | 0.043 | 0.059 |
| $^{131}\mathrm{Xe}(5/2_1^+ \to 3/2_{\mathrm{g.s.}}^+)$ | $6.62 \times 10^{-4}$ | 0.020 | 0.028 |
| $^{131}\mathrm{Xe}(3/2_2^+ \to 3/2_{\mathrm{g.s.}}^+)$ | 0.011 | 0.013 | 0.020 |
| $^{133}\mathrm{Cs}(5/2_1^+ \to 7/2_{\mathrm{g.s.}}^+)$ | $4.24 \times 10^{-3}$ | $1.39 \times 10^{-4}$ | $2.65 \times 10^{-3}$ |
| $^{133}\mathrm{Cs}(5/2_2^+ \to 7/2_{\mathrm{g.s.}}^+)$ | $2.09 \times 10^{-3}$ | $6.62 \times 10^{-3}$ | $4.93 \times 10^{-3}$ |
| $^{127}\mathrm{I}(1/2_1^+ \to 3/2_1^+)$ | 0.134 | $1.58 \times 10^{-4}$ | $7.47 \times 10^{-6}$ |
| $^{127}\mathrm{I}(5/2_2^+ \to 3/2_1^+)$ | 0.037 | 0.021 | 0.131 |
| $^{127}\mathrm{I}(5/2_2^+ \to 7/2_1^+)$ | 0.027 | 0.069 | 0.021 |
| $^{129}\mathrm{Xe}(3/2_2^+ \to 3/2_1^+)$ | $4.55 \times 10^{-3}$ | 0.011 | 0.018 |
| $^{129}\mathrm{Xe}(5/2_1^+ \to 3/2_1^+)$ | 0.018 | 0.115 | 0.153 |
| $^{131}\mathrm{Xe}(9/2_1^- \to 11/2_1^-)$ | $1.79 \times 10^{-4}$ | 0.012 | 0.013 |
| $^{131}\mathrm{Xe}(3/2_2^+ \to 1/2_1^+)$ | 0.011 | $5.15 \times 10^{-3}$ | $6.92 \times 10^{-3}$ |
| $^{133}\mathrm{Cs}(5/2_2^+ \to 5/2_1^+)$ | 0.138 | 0.014 | 0.038 |
| $^{133}\mathrm{Cs}(3/2_1^+ \to 5/2_2^+)$ | $2.60 \times 10^{-3}$ | 0.055 | 0.179 |
| $^{133}\mathrm{Cs}(3/2_1^+ \to 5/2_1^+)$ | 0.043 | 0.128 | 0.352 |

by an LLS fit to experimental magnetic moments. Because of this success, we introduce a renormalization of the proton and neutron spin operators with the renormalization factors

$$r_p = \frac{3.189}{5.586} = 0.571 \quad \text{(protons)}, \tag{1}$$

$$r_n = \frac{3.370}{3.826} = 0.881 \quad \text{(neutrons)}. \tag{2}$$

In the following we use these renormalized spin operators to compute the detection rates of elastic and inelastic LSP-nucleus scattering off the four discussed nuclei.

For completeness, we also give the calculated proton and neutron spin and orbital angular momentum matrix elements for the two lowest states in the discussed nuclei in Table III. For the $5/2^+$ ground state of $^{127}$I we can compare our results with the results of the SM calculations of Refs. [21,32]. For the xenon nuclei we quote the results of Ref, [32]. In Ref. [32] the comparison was extended to other, more rudimentary calculations for $^{127}$I, $^{129}$ Xe, and $^{131}$Xe. In Ref. [21] the same effective interaction, namely the Bonn-CD $G$ matrix, was used as here and only the truncation scheme in the calculation was different. In Ref. [32] both the Bonn-A and the Nijmegen-II interactions were used. As can be seen in Table III, all the results for the $^{127}$I ground state are similar, in particular for the leading matrix element $\langle \mathbf{L}_p \rangle$. Also for $^{131}$Xe the various SM results coincide nicely. For $^{129}$Xe there is no dominating matrix element and the results of the present calculation deviate somewhat from those of Ref. [32].

TABLE III. Calculated proton and neutron spin and orbital angular momentum matrix elements for the two lowest states in the discussed nuclei. For the ground states of $^{127}$I and the xenon nuclei we have included other SM calculations.

| State | $\langle \mathbf{S}_n \rangle$ | $\langle \mathbf{S}_p \rangle$ | $\langle \mathbf{L}_n \rangle$ | $\langle \mathbf{L}_p \rangle$ |
|---|---|---|---|---|
| $^{127}\mathrm{I}(5/2_{\mathrm{g.s.}}^+)$ | 0.030 | 0.418 | 0.867 | 1.331 |
| [21] (Bonn-CD) | 0.038 | 0.330 | 0.702 | 1.430 |
| [32] (Bonn-A) | 0.075 | 0.309 | 0.779 | 1.338 |
| [32] (Nijmegen) | 0.064 | 0.354 | 0.664 | 1.418 |
| $^{127}\mathrm{I}(7/2_1^+)$ | 0.056 | −0.327 | 0.852 | 3.093 |
| $^{129}\mathrm{Xe}(1/2_{\mathrm{g.s.}}^+)$ | 0.273 | −0.0019 | 0.113 | 0.115 |
| [32] (Bonn-A) | 0.359 | 0.028 | −0.114 | 0.227 |
| [32] (Nijmegen) | 0.300 | 0.013 | −0.185 | 0.372 |
| $^{129}\mathrm{Xe}(3/2_1^+)$ | −0.049 | −0.0034 | 1.297 | 0.256 |
| $^{131}\mathrm{Xe}(3/2_{\mathrm{g.s.}}^+)$ | −0.125 | −0.00069 | 1.417 | 0.209 |
| [32] (Bonn-A) | −0.227 | −0.009 | 1.572 | 0.165 |
| [32] (Nijmegen) | −0.217 | −0.012 | 1.514 | 0.215 |
| $^{131}\mathrm{Xe}(1/2_1^+)$ | 0.293 | −0.0034 | 0.095 | 0.116 |
| $^{133}\mathrm{Cs}(7/2_{\mathrm{g.s.}}^+)$ | 0.021 | −0.318 | 0.448 | 3.524 |
| $^{133}\mathrm{Cs}(5/2_1^+)$ | 0.013 | 0.391 | 0.348 | 1.893 |

## III. RESULTS FOR THE ELASTIC SCATTERING RATES

In Ref. [21] a derivation was given for the event rate of elastic LSP scattering off an Earth-bound detector. The final result could be written as

$$\langle R \rangle_{\mathrm{el}} = \left[ \left(f_A^0\right)^2 D_1 + 2 f_A^0 f_A^1 D_2 + \left(f_A^1\right)^2 D_3 + A^2 \left( f_S^0 - f_S^1 \frac{A-2Z}{A} \right)^2 D_4 \right] m_{\mathrm{det}}[\mathrm{kg}], \tag{3}$$

where $m_{\mathrm{det}}[\mathrm{kg}]$ is the detector mass in units of kilograms, $A$ is the mass number of the target nucleus, and the $f$ coefficients are specific to the chosen SUSY model [25,40]. The coefficients $D_n$ are folded with the symmetric Maxwell-Boltzmann velocity distribution of the LSPs expressed as

$$f(\mathbf{v}, \mathbf{v}_E) = (\sqrt{\pi} v_0)^{-3} e^{-(\mathbf{v}+\mathbf{v}_E)^2/v_0^2}, \tag{4}$$

where $\mathbf{v}_E$ is the velocity of the Earth with respect to the galactic center and $\mathbf{v}$ is the velocity of the LSP particle with respect to the LSP detector. The velocity $\mathbf{v}_E$ can be written as

$$\mathbf{v}_E = \mathbf{v}_0 + \mathbf{v}_1, \tag{5}$$

where $\mathbf{v}_0$ denotes the Sun's velocity in galactic coordinates and $\mathbf{v}_1$ denotes the Earth's velocity with respect to the Sun.

The coefficients $D_n$ contain all the information about the nuclear structure. They are defined as

$$D_1 = \int_{-1}^{+1} \int_{\psi_{\min}}^{\psi_{\max}} \int_{u_{\min}}^{u_{\max}} G(\psi, \xi) F_{00}(u) \Omega_0^2 d\xi d\psi du, \tag{6}$$

$$D_2 = \int_{-1}^{+1} \int_{\psi_{\min}}^{\psi_{\max}} \int_{u_{\min}}^{u_{\max}} G(\psi, \xi) F_{01}(u) \Omega_0 \Omega_1 d\xi d\psi du, \tag{7}$$

$$D_3 = \int_{-1}^{+1} \int_{\psi_{\min}}^{\psi_{\max}} \int_{u_{\min}}^{u_{\max}} G(\psi,\xi) F_{11}(u) \Omega_1^2 d\xi d\psi du, \quad (8)$$

$$D_4 = \int_{-1}^{+1} \int_{\psi_{\min}}^{\psi_{\max}} \int_{u_{\min}}^{u_{\max}} G(\psi,\xi) |F(u)|^2 d\xi d\psi du, \quad (9)$$

where $F(u)$ is the nuclear form factor [25] and $F_{\rho\rho'}(u)$, $\rho, \rho' = 0, 1$ are the usual spin structure functions

$$F_{\rho\rho'} = \sum_{\lambda,\kappa} \frac{\Omega_\rho^{(\lambda,\kappa)}(u) \Omega_{\rho'}^{(\lambda,\kappa)}(u)}{\Omega_\rho \Omega_{\rho'}}, \quad (10)$$

where

$$\Omega_\rho = \Omega_\rho^{(0,1)}(0) \quad (11)$$

are the static spin matrix elements and

$$\Omega_\rho^{(\lambda,\kappa)}(u) = \sqrt{\frac{4\pi}{2J_i+1}} \left( J_f \| \sum_{j=1}^{A} [\mathbf{Y}_\lambda(\Omega_j) \otimes \boldsymbol{\sigma}]_\kappa j_\lambda(\sqrt{u} r_j) \omega_\rho(j) \| J_i \right), \quad (12)$$

with $\omega_0(j) = 1$ and $\omega_1(j) = \tau_3(j)$. The angles $\Omega_j$ are the solid angles for the position vectors of the nucleons, $\mathbf{Y}_\lambda$ is a spherical harmonic, $\boldsymbol{\sigma}$ is the Pauli spin matrix, and $j_\lambda$ is a spherical Bessel function. The variable $u$ is related to the momentum transfer to the nuclear target, $q$, by

$$u = q^2 b^2/2, \quad (13)$$

where $b$ is the nuclear harmonic oscillator size parameter obtained from the nuclear mass number $A$ as described,for example, in Ref. [41].

The expression for the modulation function $G(\psi,\xi)$ is given by

$$G(\psi,\xi) = \frac{\rho(0)}{m_\chi} \frac{\sigma_0}{A m_p} \left( \frac{1}{m_p b} \right)^2 \frac{e^{-\lambda^2}}{\sqrt{\pi}} \frac{c^2}{v_0} \psi e^{-\psi^2} e^{-2\lambda\psi\xi}, \quad (14)$$

with $\psi = v/v_0$ and $\lambda = v_E/v_0$. Here $\sigma_0 = 0.77 \times 10^{-38}$ cm$^2$, $m_\chi$ is the mass of the LSP, $\rho(0) = 0.3$ GeV/cm$^3$ is the LSP density near Earth, $m_p$ is the proton rest mass, $A$ is the nuclear mass number, $c$ is the velocity of light, $v$ is the speed of the LSP relative to the Earth-bound detector, and $v_0 = 220$ km/s is the circulation speed of the Sun around the galactic center. The speed of Earth with respect to the galactic center can be expressed as

$$v_E = \sqrt{v_0^2 + v_1^2 + 2 v_0 v_1 \sin\gamma \cos a}, \quad (15)$$

where $\gamma = 29.80^\circ$, $a$ represents the phase of the Earth [25], and $v_1$ is Earth's speed with respect to the Sun. The upper limit of the integration over $\psi$ can be obtained from the upper bound $v_{\rm esc} = 625$ km/s for the speed $|\mathbf{v} + \mathbf{v}_E|$ of the LSP in galactic coordinates. This leads to the inequality

$$|\mathbf{v} + \mathbf{v}_E|^2 = v^2 + v_1^2 + v_0^2 + 2\mathbf{v}\cdot\mathbf{v}_E + 2\mathbf{v}_0\cdot\mathbf{v}_1 < v_{\rm esc}^2. \quad (16)$$

We then obtain the following limits:

$$\psi_{\min} = \frac{c}{v_0} \left( \frac{Q_{\rm thr}}{2\mu_r} \right)^{1/2}, \quad (17)$$

$$\psi_{\max} = -\lambda\xi + \sqrt{\lambda^2\xi^2 + 7.05 - 0.135\cos a}, \quad (18)$$

$$u_{\min} = \mu_r Q_{\rm thr} b^2, \quad (19)$$

$$u_{\max} = 2(\psi \mu_r b v_0/c)^2, \quad (20)$$

where $Q_{\rm thr}$ is the detector threshold energy and $\mu_r$ is the reduced mass of the LSP-nucleus system.

The nuclear form factor $F(u)$ we evaluate directly by using our nuclear wave functions. The usual way to avoid this computationally demanding task is to simply start from the nuclear mass distribution without going into details of the many-body physics behind this distribution. Since the nuclear mass distribution is hard to measure it is assumed that it is of the same form as the experimentally well known nuclear charge distribution. A suitably smoothed mass distribution gives a simple analytical expression for the nuclear form factor. The most used form factor of this kind is the Helm form factor [42]. This form factor can be improved by using the elastic electron scattering data, as shown in Ref. [43].

The static spin matrix elements (SSME), present in Eqs. (6)–(8), are reviewed in Table IV for both the elastic and inelastic scattering channels and for all the discussed nuclei. Variations in the values of the $g$ factors induce variations in the values of the final computed SSMEs as seen in Table IV. For $^{127}$I and $^{133}$Cs the bare and fitted results for the SSMEs deviate substantially (some 40%–50%) from each other. This is not the case for $^{129}$Xe and $^{131}$Xe where the deviation is only of the order of 12%. This difference between the two groups of nuclei is understandable if one notices that the biggest improvements in the computed magnetic moments occur for $^{127}$I and $^{133}$Cs, as seen in Table I. For $^{129}$Xe and $^{131}$Xe the improvements are minor.

The differences in the final computed $D$ coefficients [Eqs. (6)–(8)], when going from the bare to the effective $g$ factors, is a reduction of the order of 20% for $^{129}$Xe and $^{131}$Xe. For $^{127}$I and $^{133}$Cs the reduction amounts to a factor of 1/3 owing to the big changes in the values of the computed magnetic moments when using the effective $g$ factors. This leads to the conclusion that the manipulation of the $g$ factors causes roughly a 20% variation in the values of the relevant LSP-nucleus scattering observables for $^{129}$Xe and $^{131}$Xe and roughly a factor of 3 for $^{127}$I and $^{133}$Cs.

TABLE IV. Calculated results for the static spin matrix elements of the discussed nuclei. The results are given for both the bare and effective $g$ factors.

| Nucleus | $g$ factors | Elastic | | Inelastic | |
|---|---|---|---|---|---|
| | | $\Omega_0$ | $\Omega_1$ | $\Omega_0$ | $\Omega_1$ |
| $^{127}$I | Bare | 1.001 | 0.868 | 0.098 | 0.066 |
| | Effective | 0.592 | 0.475 | 0.061 | 0.033 |
| $^{129}$Xe | Bare | 0.941 | −0.954 | 0.306 | −0.311 |
| | Effective | 0.831 | −0.838 | 0.270 | −0.273 |
| $^{131}$Xe | Bare | −0.326 | 0.322 | 0.236 | −0.224 |
| | Effective | −0.286 | 0.284 | 0.206 | −0.199 |
| $^{133}$Cs | Bare | 0.643 | 0.732 | 0.059 | 0.050 |
| | Effective | 0.353 | 0.432 | 0.035 | 0.027 |

The SSME values for $^{127}$I, obtained in Ref. [21] for the elastic channel and bare $g$ factors, were $\Omega_0 = 0.871$ and $\Omega_1 = 0.690$. The difference between these values and the present ones stems from the different truncation schemes. In Ref. [21] at most six neutrons were allowed to be in the $0h_{11/2}$ orbital and here we allow at most one-particle-one-hole excitations from the full $1d_{5/2}$ and $0g_{7/2}$ shells. In the present calculation we had to resort to a more severe truncation than in Ref. [21] since we wanted to calculate also the $^{129}$Xe, $^{131}$Xe, and $^{133}$Cs nuclei on the same footing, posing no restrictions to the proton configurations.

In the case of $^{127}$I for the elastic channel our results $\Omega_0^2 = 0.350$ and $\Omega_1^2 = 0.226$ using effective $g$ factors are rather close to the values of Refs. [30,31,34]. For our bare $g$ factors and the calculation of Ref. [32] these quantities assume notably bigger values. For this duality of the results it is hard to judge the reliability of the present calculation for $^{127}$I. The differences might be associated with possible deformation effects, as discussed in more detail in the context of inelastic scattering in the next section. For the xenon isotopes the elastic channel seems to be well described when the effective $g$ factors are used: The calculated magnetic moments agree nicely with the measured ones. For $^{133}$Cs the effective $g$ factors produce very good magnetic moments and the description of elastic LSP-nucleus scattering seems rather reliable. Discussion of the SSME values for inelastic scattering is postponed to the next section.

In Fig. 3 we plot the spin structure functions $F_{\rho\rho'}(u)$ and the nuclear form factor $|F(u)|^2$ as functions of the momentum transfer $u$ for elastic LSP-nucleus scattering on $^{127}$I (upper panels) and $^{133}$Cs (lower panels). For the most relevant, small $u$ values we have a added linear scale on the right panels. As can be seen the nuclear form factor and the spin structure functions (SSFs) behave very similarly for small $u$ (right panels) but

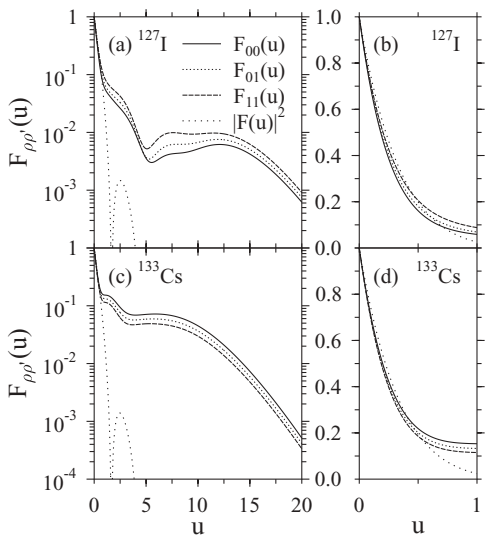


FIG. 3. Spin structure functions $F_{\rho\rho'}(u)$ and the nuclear form factor $|F(u)|^2$ plotted as functions of the momentum transfer $u$ for elastic LSP-nucleus scattering on $^{127}$I (a) and $^{133}$Cs (c). For the important small $u$ values we have added a linear scale in panels (b) and (d).

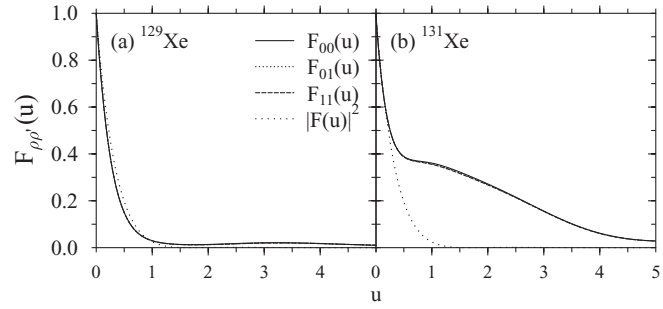


FIG. 4. Spin structure functions $F_{\rho\rho'}(u)$ and the nuclear form factor $|F(u)|^2$ plotted as functions of the momentum transfer $u$ for elastic LSP-nucleus scattering on $^{129}$Xe (a) and $^{131}$Xe (b).

beyond that the behavior of the nuclear form factor differs drastically from that of the SSFs.

In Fig. 4 we plot the SSFs and the nuclear form factor as functions of the momentum transfer $u$ for elastic LSP-nucleus scattering on $^{129}$Xe [Fig. 4(a)] and $^{131}$Xe [Fig. 4(b)]. For $^{129}$Xe all the curves behave in an identical way, but for $^{131}$Xe the form factor behaves differently from the SSFs. Here it is appropriate to note that in many other works (e.g., Refs. [29,32]), the SSFs $F_{\rho\rho'}(u)$ for the elastic scattering are replaced by the $S_{\rho\rho'}(q)$ functions. These functions can be derived from the $F$ functions by the conversion formulas

$$S_{00}(q) = \frac{2J_{\text{g.s.}}+1}{16\pi}\Omega_0^2 F_{00}(u), \tag{21}$$

$$S_{01}(q) = \frac{2J_{\text{g.s.}}+1}{8\pi}\Omega_0\Omega_1 F_{01}(u), \tag{22}$$

$$S_{11}(q) = \frac{2J_{\text{g.s.}}+1}{16\pi}\Omega_1^2 F_{11}(u), \tag{23}$$

where $J_{\text{g.s.}}$ is the ground-state spin of the target nucleus.

The $D_n$ factors of Eqs. (6)–(9) (in units of yr$^{-1}$ kg$^{-1}$) are plotted in Figs. 5–8 as functions of the LSP mass for the nuclei under discussion. The factors are given for three different values of the detector threshold energy $Q_{\text{thr}}$. In the plots the seasonal variation in the detection rate (annual modulation) is presented by the thickness of the line. The associated computations were done by assuming the effective $g$ factors.

All four $D_n$ factors, for all the discussed nuclei, show the same qualitative pattern, that is, a maximum at around $m_\chi =$ 30 GeV ($^{127}$I, $^{129}$Xe, $^{133}$Cs) or $m_\chi =$ 30–90 GeV ($^{131}$Xe) and then a decaying tail approaching zero for large LSP masses. Only for $^{131}$Xe does the position of the maximum depend notably on the threshold energy $Q_{\text{thr}}$. The magnitudes of the spin-dependent coefficients $D_1$, $D_2$, and $D_3$ are by far the largest for $^{129}$Xe, the nucleus $^{127}$I having the next biggest spin-dependent coefficients and $^{131}$Xe the smallest ones.

## IV. RESULTS FOR THE INELASTIC SCATTERING RATES

Following the lines of derivation of the elastic event rate in Ref. [21] we can write for the event rate of the inelastic LSP-nucleus scattering as

$$\langle R\rangle_{\text{inel}} = \left[\left(f_A^0\right)^2 E_1 + 2 f_A^0 f_A^1 E_2 + \left(f_A^1\right)^2 E_3\right] m_{\text{det}}[\text{kg}]. \tag{24}$$

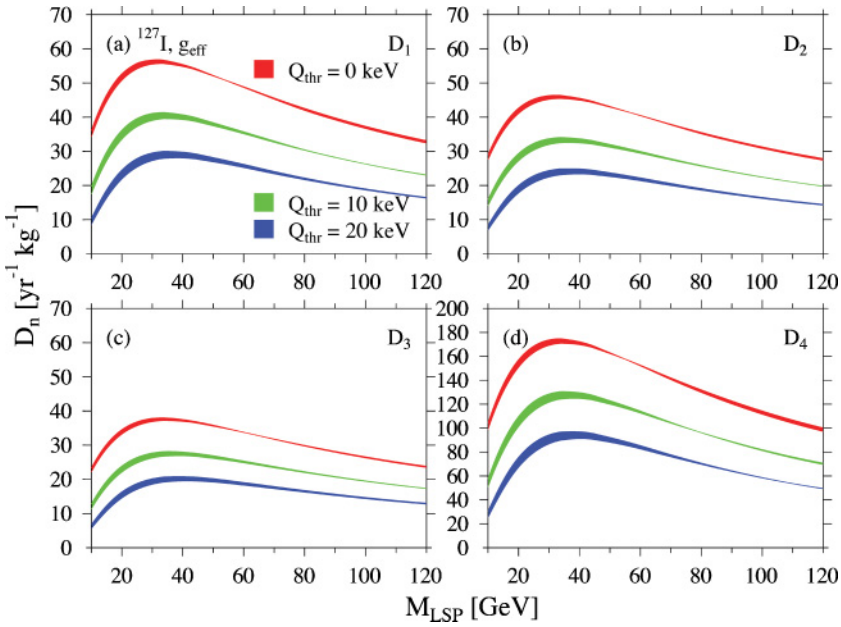


FIG. 5. (Color online) The $D_n$ factors of Eqs. (6)–(9), in units of yr$^{-1}$ kg$^{-1}$, plotted as functions of the LSP mass for three different threshold energies in the case of elastic scattering of the LSP off an $^{127}$I nucleus: (a) $D_1$, (b) $D_2$, (c) $D_3$, and (d) $D_4$. The thickness of the curves describes the annual modulation effect.

Here we assume the same folding procedure with the LSP velocity distribution as in the case of elastic scattering. It is to be noted that here we have denoted the coefficients $D_i, i = 1, 2, 3$, of our previous Letter [26] with the symbols $E_i, i = 1, 2, 3$, to better distinguish between the elastic and inelastic channels. Hence, for these coefficients we have

$$E_1 = \int_{-1}^{+1} \int_{\psi_{\min}}^{\psi_{\max}} \int_{u_{\min}}^{u_{\max}} G(\psi, \xi) F_{00}(u) \Omega_0^2 d\xi d\psi du, \quad (25)$$

$$E_2 = \int_{-1}^{+1} \int_{\psi_{\min}}^{\psi_{\max}} \int_{u_{\min}}^{u_{\max}} G(\psi, \xi) F_{01}(u) \Omega_0 \Omega_1 d\xi d\psi du, \quad (26)$$

$$E_3 = \int_{-1}^{+1} \int_{\psi_{\min}}^{\psi_{\max}} \int_{u_{\min}}^{u_{\max}} G(\psi, \xi) F_{11}(u) \Omega_1^2 d\xi d\psi du. \quad (27)$$

We define the SSMEs for the inelastic scattering in the same way as done for the elastic one [i.e., through Eqs. (11) and (12)]. The SSMEs for the inelastic channel, present in Eqs. (25)–(27), are given in Table IV for the nuclei under discussion. Whereas for $^{129}$Xe and $^{131}$Xe the inelastic SSMEs are of the same order of magnitude as the elastic ones, for $^{127}$I and $^{133}$Cs they are at least an order of magnitude smaller than the elastic SSMEs. This difference between the two groups of nuclei stems from the nuclear wave functions since the SSMEs contain the associated transition densities. There is no explicit dependence on excitation energy for the SSMEs; the excitation energy plays a role only in the integration limits of the $D_n$ coefficients. By their larger SSMEs $^{129}$Xe and $^{131}$Xe are potentially more sensitive to inelastic LSP-nucleus scattering than $^{127}$I and $^{133}$Cs.

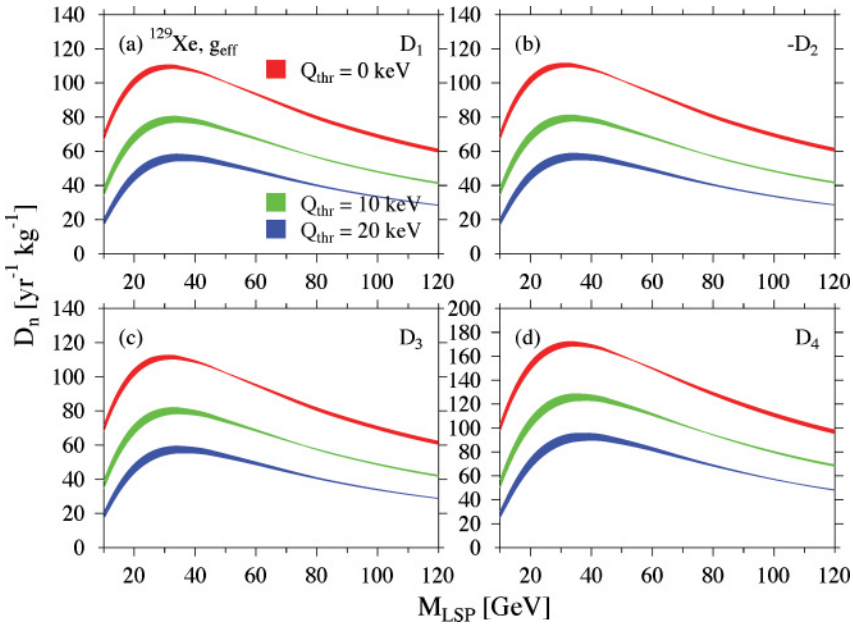


FIG. 6. (Color online) The same as in Fig. 5 for elastic scattering of the LSP off a $^{129}$Xe nucleus. Here panel (b) shows $-D_2$.

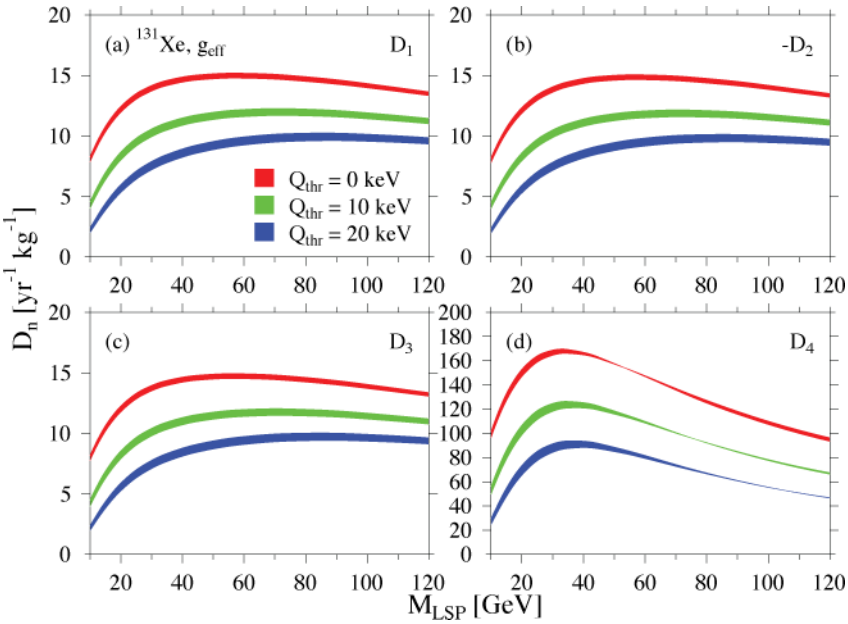


FIG. 7. (Color online) The same as in Fig. 5 for elastic scattering of the LSP off a $^{131}$Xe nucleus. Here panel (b) shows $-D_2$.

In the case of $^{127}$I we can compare our results with the ones of Ref. [34] for the inelastic channel. Our results $\Omega_0^2 = 0.0096$ (bare $g$ factors) and $\Omega_0^2 = 0.0037$ (effective $g$ factors) deviate drastically from the value $\Omega_0^2 = 0.312$ obtained in Ref. [34] where deformed Nilsson single-particle wave functions were used in a simplified calculational scheme for oblate deformation. The reason for this difference might be in the difficulty of the shell model in taking into account a possible deformation. This difficulty is already seen in Table III where the shell model predicts the strength $B(M1; 7/2_1^+ \rightarrow 5/2_{g.s.}^+)$ to be a factor of 4.4 (bare $g$ values) and 26 (effective $g$ values) too weak. This rough factor of 6 difference in the two shell-model calculations induces a factor of 2.6 difference in the corresponding $\Omega_0^2$ values. Unfortunately, in Ref. [34] the relevant $B(M1)$ value was not given for comparison. It is interesting to note, though, that the magnetic moments of the involved states are predicted quite nicely by the SM, as seen in Table I. In any case, the role of deformation in this context is worth studying in possible future work.

For the xenon isotopes the SM predicted $B(M1; 3/2_1^+ \rightarrow 1/2_{g.s.}^+)$ ($^{129}$Xe) and $B(M1; 1/2_1^+ \rightarrow 3/2_{g.s.}^+)$ ($^{131}$Xe) values are in excellent agreement with the data, so that the SSME for the inelastic channel should be quite reliable. For $^{133}$Cs the calculated $B(M1; 5/2_1^+ \rightarrow 7/2_{g.s.}^+)$ for the bare $g$ factors is close to the corresponding measured number but the value calculated by using the effective $g$ factors is clearly off. Interestingly enough, this large difference of a factor 19 in the computed $B(M1)$ values induces only a difference of a

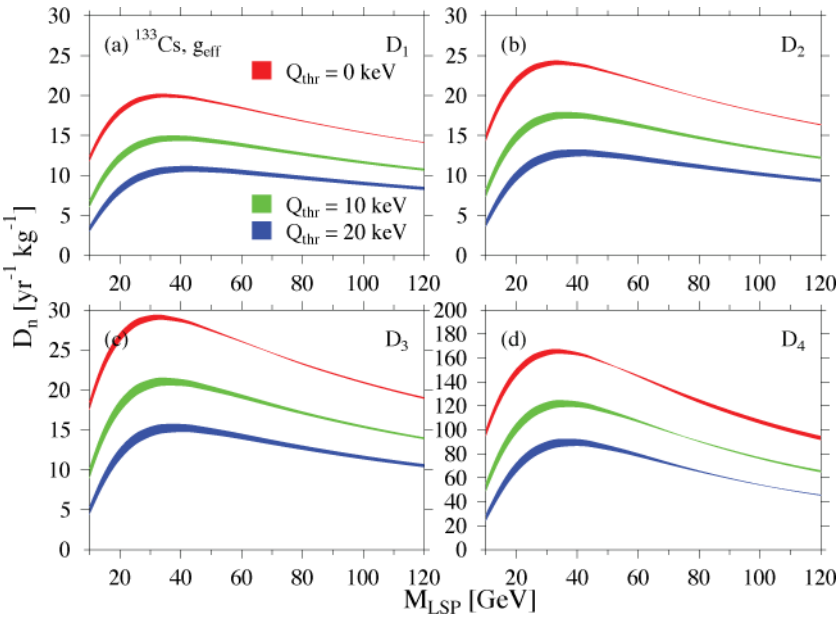


FIG. 8. (Color online) The same as in Fig. 5 for elastic scattering of the LSP off a $^{133}$Cs nucleus.

factor of 2.8 in the values of $\Omega_0^2$ for the inelastic channel. In this case, like in the case of $^{127}$I, the role of deformation is an interesting subject for further studies.

At this point one could ask whether the used single-particle space is big enough to produce reliable values for the physical observables relevant for the LSP-nucleus scattering. Most likely the space is enough for quantities to which the calculations give values that are of the same order of magnitude as the corresponding results for the extreme single-particle shell model. These are quantities that are not suppressed relative to simple estimates, as is the case for our results for the xenon nuclei. If the computed values of observables are much suppressed relative to the "standard" values, as happens in several cases for $^{127}$I and $^{133}$Cs, it could be that contributions coming from outside the chosen single-particle space become important. Unfortunately, at the moment we do not know how to estimate this effect in our calculations, as discussed in the following.

It could be that the presently used effective interaction is not at its best for systems that have very large neutron excess. One then would like to extend the size of the active model space of the calculation. One possibility would be to activate the $0g_{9/2}$ orbital and add it to the model space (e.g., by considering particle-hole excitations from it up to the presently used model space). The most restricted version of this extension of the calculation would be to consider the $0g_{9/2}$ to $0g_{7/2}$ 1p-1h excitations. Unfortunately, we could not estimate the effect of these particle-hole excitations for two reasons. First, the model space would have become too large (being already very big for a SM calculation), and second, we did not have a suitable effective interaction available for that kind of model space. We have used an effective interaction that divides the full unrestricted model space into two regions: a P-space, which consists of the $2s_{1/2}$, $1d_{5/2}$, $1d_{3/2}$, $0g_{7/2}$, and $0h_{11/2}$ orbitals, and a Q-space, which contains everything else ($^{100}$Sn core plus unoccupied orbitals beyond our valence space). Hence P + Q gives the full Hilbert space. The 1p-1h excitations from the core to the P-space (core polarization) and from the P-space to the Q-space above the P-space have been taken into account approximately by the effective interaction equations as described in Ref. [38]. Thus, including these 1p-1h excitations in the present SM calculation would introduce uncontrollable double counting. In the light of this problem, the extension of the interaction to include the $0g_{9/2}$ orbital into the P-space, as well as the subsequent massive SM calculation, has to be left for future work with future computers.

In Fig. 9 we plot the SSFs $F_{\rho\rho'}(u)$ of Eq. (10) as functions of the momentum transfer $u$ for inelastic LSP-nucleus scattering on $^{127}$I [Fig. 9(a)] and $^{133}$Cs [Fig. 9(c)]. The important low $u$ values are shown in Figs. 9(b) and 9(d). The SSFs differ from each other much more than in the case of the elastic scattering in Fig. 3. In addition, for elastic scattering the SSFs *drop* fast below one but for inelastic scattering these functions *grow* fast in the beginning and stay above unity for the range $u \leqslant 5$.

The reason for this described behavior of the SSFs is the following. For inelastic scattering on $^{127}$I and $^{133}$Cs the proton one-body transition densities (OBTDs) between the single-particle orbitals $1d_{5/2}$ and $0g_{7/2}$, for the $\kappa = 1$ multipole [see Eq. (12)], are much stronger than the other OBTDs. For $u > 0$ these OBTDs affect strongly the SSFs through the

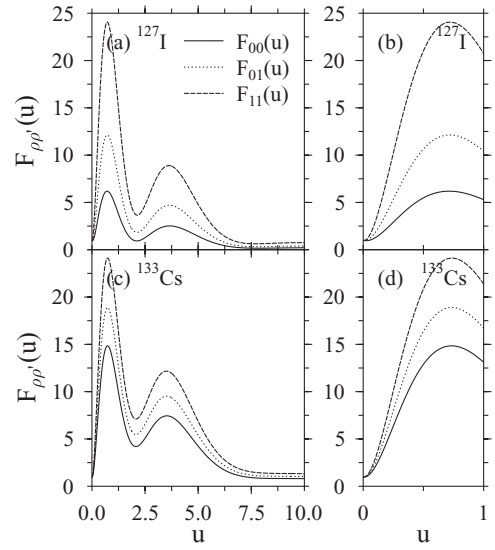


FIG. 9. Spin structure functions $F_{\rho\rho'}(u)$ plotted as functions of the momentum transfer $u$ for inelastic LSP-nucleus scattering on $^{127}$I [(a) and (b)] and $^{133}$Cs [(c) and (d)].

$\lambda = 2$ channel [see again Eq. (12)]. It is notable that these very strong OBTDs do not contribute to the SSMEs $\Omega_0$ and $\Omega_1$ because of the angular momentum couplings and the zero $j_2(0) = 0$ of the spherical Bessel function $j_2$. Owing to angular momentum algebra these OBTDs do not contribute to the $M1$ transitions, either. This observation means that one cannot relate the $M1$ transitions directly to the LSP-nucleus inelastic matrix elements as done in Ref. [35].

In Fig. 10 we plot the SSFs as functions of $u$ for inelastic scattering on $^{129}$Xe [Fig. 10(a)] and $^{131}$Xe [Fig. 10(b)]. The differences in the plots between the xenon nuclei and $^{127}$I and $^{133}$Cs are rather drastic. Whereas for $^{127}$I and $^{133}$Cs the SSFs grow fast for small $u$, for the xenons the SSFs drop below one. For $^{127}$I and $^{133}$Cs the SSFs stay above unity for the range $u \leqslant 5$ whereas for the xenon nuclei they drop to the $10^{-4}$ level within this range [26]. Hence, for the $^{127}$I and $^{133}$Cs nuclei the SSFs have values that are much bigger than for the xenon nuclei. The pronounced bump in the SSF of $^{131}$Xe [Fig. 10(b)] stems from the very strong neutron transition $1d_{3/2} \rightarrow 2s_{1/2}$ for multipole $\kappa = 2$ in Eq. (12). For $\lambda = 2$ the radial integral over these orbitals and the associated Bessel function attains its maximum around the bump region.

Let us next discuss how to obtain the lower and upper limits for the integrals in Eqs. (25)–(27). The upper limit of the integration over $\psi = v/v_0$ is obtained in the same way as for the case of elastic LSP-nucleus scattering. In the present work we do not take into account the rotation of Earth on its axis. Hence, for the upper limit of $\psi$ we obtain the expression given by Eq. (18).

The other integration limits can be obtained as follows. For the initial and final kinetic energies of the LSP ($E_\chi^i$, $E_\chi^f$) and the nucleus ($E_N^i$, $E_N^f$) we can write

$$E_\chi^i + E_N^i = E^* + E_\chi^f + E_N^f, \tag{28}$$

where $E^*$ represents the excitation energy of the nucleus in its final state. In the center-of-mass system (CMS) one can write

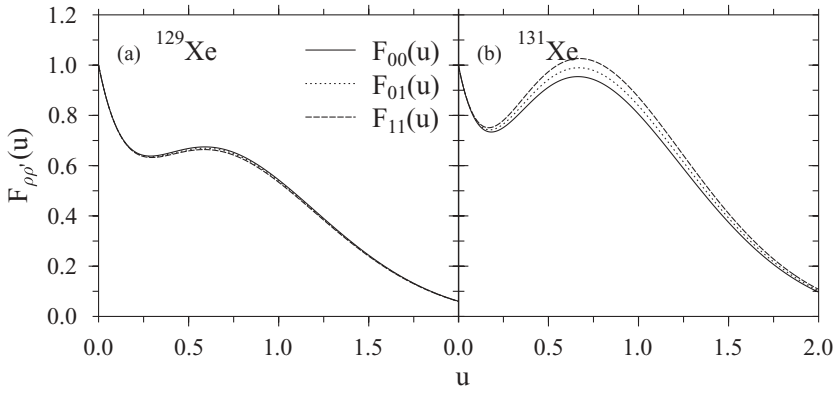


FIG. 10. Spin structure functions $F_{\rho\rho'}(u)$ plotted as functions of the momentum transfer $u$ for inelastic LSP-nucleus scattering on $^{129}$Xe (a) and $^{131}$Xe (b).

the square of the exchanged three-momentum as

$$\mathbf{q}^2 = 2m_\chi\left(E^i_\chi + E^f_\chi\right) - 2m_\chi v'^i_\chi\, v'^f_\chi \cos\theta, \tag{29}$$

where $v'^i_\chi$ are $v'^f_\chi$ are, respectively, the initial and final speeds of the LSP in the CMS and $m_\chi$ is its rest mass. The maximum exchanged momentum $q^2_{\max}$ occurs at $\cos\theta = -1$. In the CMS $m_\chi v'^f_\chi = -m_N v'^f_N$, which leads to $E^f_\chi = (m_N/m_\chi)E^f_N$. Thus one can write

$$E^f_\chi = \frac{m_N}{m_N + m_\chi}\left(E^i_N + E^i_\chi - E^*\right). \tag{30}$$

This equation can be inserted into Eq. (29) to yield

$$q^2_{\max} = m^2_\chi\left(v'^i_\chi\right)^2\left[1 + \sqrt{1 - \frac{2\mu_r E^*}{\left(m_\chi v'^i_\chi\right)^2}}\right]^2, \tag{31}$$

where $\mu_r$ is the reduced mass of the LSP-nucleus system. The velocity $v'^i_\chi$ can be written in terms of the corresponding laboratory velocity $v^i_\chi$ as

$$v'^i_\chi = v^i_\chi - V_{\rm CMS} = v^i_\chi \frac{m_N}{m_N + m_\chi}. \tag{32}$$

By inserting this into Eq. (31) one finally obtains

$$q^2_{\max} = \mu^2_r\left(v^i_\chi\right)^2\left[1 + \sqrt{1 - \frac{2E^*}{\mu_r\left(v^i_\chi\right)^2}}\right]^2. \tag{33}$$

The derivation for $q^2_{\min}$ is similar; one just takes $\cos\theta = +1$. This leads to the result

$$q^2_{\min} = \mu^2_r\left(v^i_\chi\right)^2\left[1 - \sqrt{1 - \frac{2E^*}{\mu_r\left(v^i_\chi\right)^2}}\right]^2. \tag{34}$$

Keeping in mind the definition of $\psi$ and noting that $u = q^2b^2/2$, where $b$ is the nuclear harmonic-oscillator size parameter, we obtain finally

$$u_{\min} = \frac{1}{2}b^2\mu^2_r\frac{v^2_0}{c^2}\psi^2[1 - \sqrt{1 - \Gamma/\psi^2}]^2, \tag{35}$$

$$u_{\max} = \frac{1}{2}b^2\mu^2_r\frac{v^2_0}{c^2}\psi^2[1 + \sqrt{1 - \Gamma/\psi^2}]^2, \tag{36}$$

where

$$\Gamma = \frac{2E^*}{\mu_r c^2}\frac{c^2}{v^2_0}. \tag{37}$$

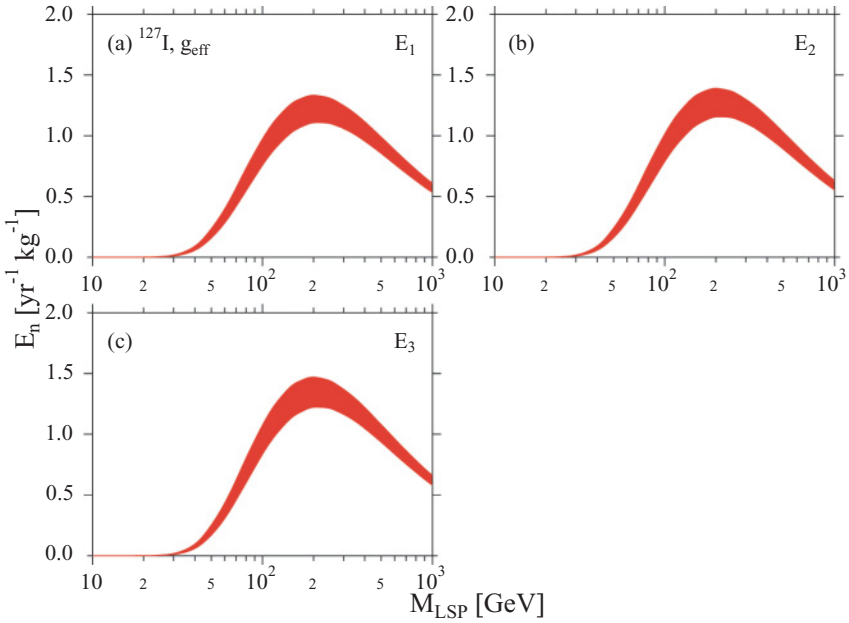


FIG. 11. (Color online) The $E_n$ factors of Eqs. (25)–(27), in units of yr$^{-1}$ kg$^{-1}$, plotted as functions of the LSP mass for inelastic scattering of the LSP off an $^{127}$I nucleus: (a) $E_1$, (b) $E_2$, and (c) $E_3$. The thickness of the curves describes the annual modulation effect.

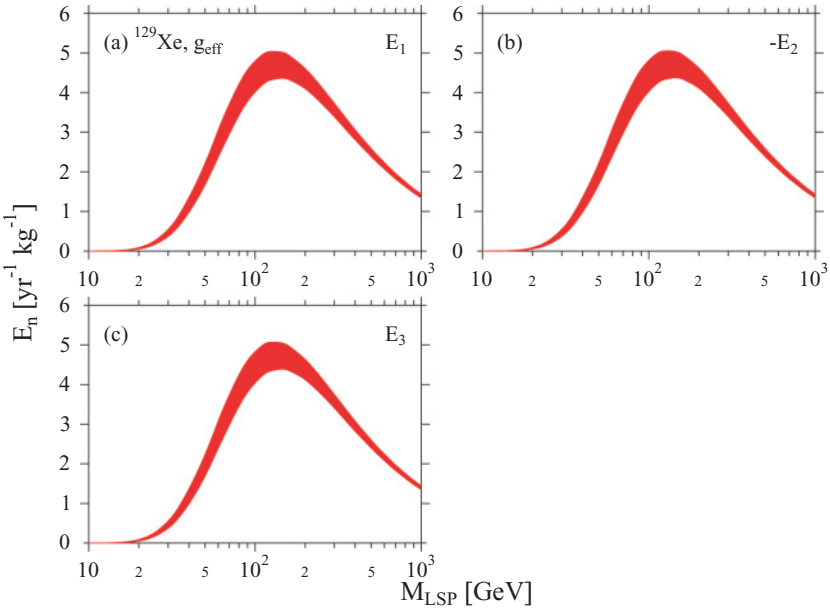


FIG. 12. (Color online) The same as in Fig. 11 for inelastic scattering of the LSP off a $^{129}$Xe nucleus. Here panel (b) shows $-E_2$.

For $\psi_{\min}$ we obtain

$$\psi_{\min} = \sqrt{\Gamma}. \tag{38}$$

It is worth noting that at the limit $E^* \to 0$ the values of $u_{\min}$ and $u_{\max}$ go to the corresponding ones of elastic scattering with $Q_{\text{thr}} = 0$.

The $E_n$ factors of Eqs. (25)–(27) (in units of yr$^{-1}$ kg$^{-1}$) are plotted in Figs. 11–14 as functions of the LSP mass for the nuclei under discussion. In the plots the seasonal variation in the detection rate (annual modulation) is presented as in the case of the elastic scattering in Figs. 5–8. For the computation we have adopted the effective $g$ factors. All the $E_n$ coefficients for all the discussed nuclei behave qualitatively in the same way (i.e., they have a maximum at around $m_\chi = 150$–300 GeV, depending on the detector nucleus). These maxima occur for about one order of magnitude heavier LSPs than in the case of the maxima of elastic scattering.

Finally, it may be of interest to study the branching ratio

$$\text{BRR} = \frac{\langle R \rangle_{\text{inel}}}{\langle R \rangle_{\text{el}} + \langle R \rangle_{\text{inel}}} \tag{39}$$

to the inelastic channel. As can be seen from Eqs. (3) and (24) the BRR depends on the SUSY parameters $f$. To have a rough idea of the suppression of the inelastic channel relative to the elastic channel one can plot the ratios of the individual $D_n$ and $E_n$ coefficients,

$$\text{BRR}_n = \frac{E_n}{D_n + E_n}, \quad n = 1, 2, 3, \tag{40}$$

as functions of the LSP mass. This has been done in Fig. 15 for the nuclei of interest and for $Q_{\text{thr}} = 0$. As can be seen, all

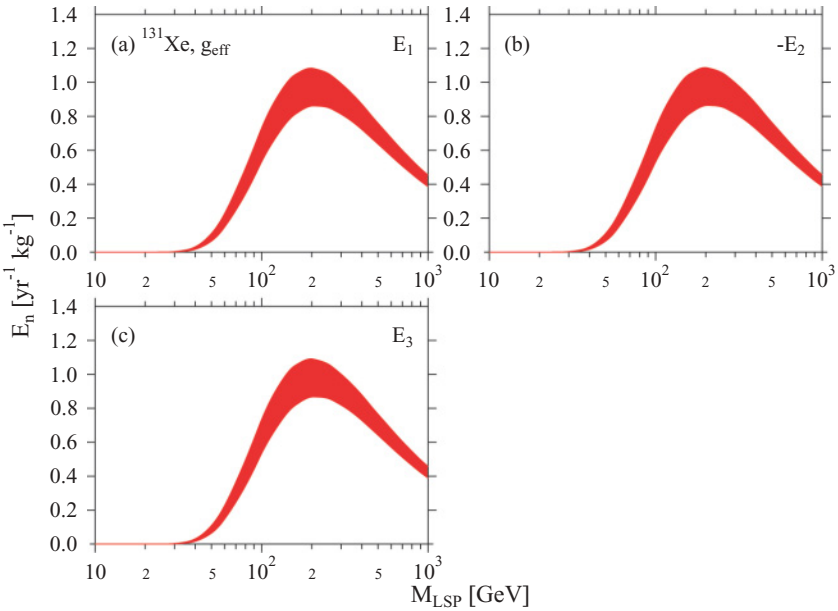


FIG. 13. (Color online) The same as in Fig. 11 for inelastic scattering of the LSP off a $^{131}$Xe nucleus. Here panel (b) shows $-E_2$.

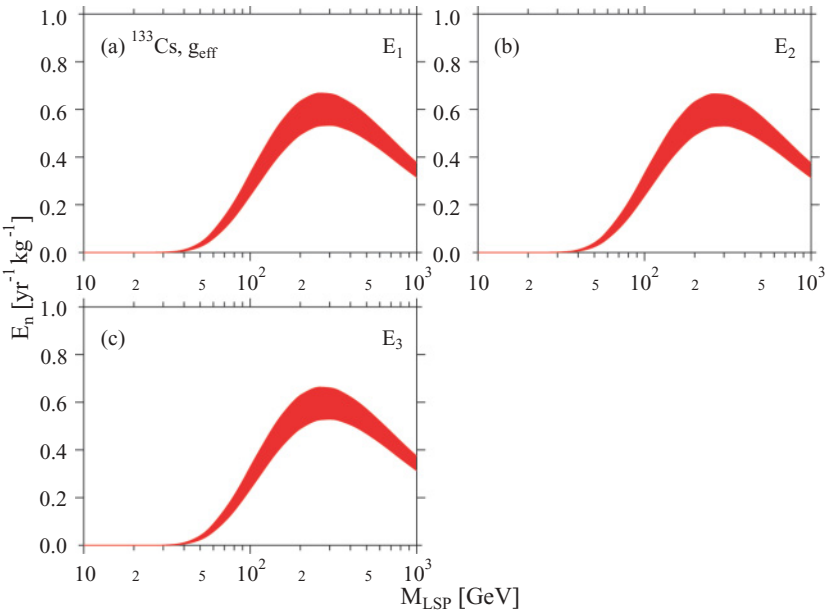


FIG. 14. (Color online) The same as in Fig. 11 for inelastic scattering of the LSP off a $^{133}$Cs nucleus.

the branching ratios $\mathrm{BRR}_n$ are quite small (at most of the order of 0.1). In addition, one has to bear in mind that a considerable contribution of the elastic rate comes from the $D_4$ term of Eq. (3), which further suppresses the branching given by Eq. (39).

## V. RESULTS FOR THE ANNUAL MODULATION

One can rewrite the Eqs. (3) and (24) by explicitly separating the annual-averaged parts, $\bar{D}_n$ and $\bar{E}_n$, and the oscillating parts, $M_n$, in each of the coefficients $D_n$ and $E_n$ according to Eq. (22) of Ref. [21]. The rewritten expressions read

$$\langle R \rangle = (r_0 + r_1 \cos a) m_{\mathrm{det}} [\mathrm{kg}]. \tag{41}$$

The $r_0$ and $r_1$ amplitudes can be written for the *elastic* channel as

$$r_0^{\mathrm{el}} = \sum_{n=1}^{4} f_n \bar{D}_n(m_\chi, Q_{\mathrm{thr}}), \tag{42}$$

$$r_1^{\mathrm{el}} = \sum_{n=1}^{4} f_n \bar{D}_n(m_\chi, Q_{\mathrm{thr}}) M_n(m_\chi, Q_{\mathrm{thr}}), \tag{43}$$

and for the *inelastic* channel we get

$$r_0^{\mathrm{inel}} = \sum_{n=1}^{3} f_n \bar{E}_n(m_\chi), \tag{44}$$

$$r_1^{\mathrm{inel}} = \sum_{n=1}^{3} f_n \bar{E}_n(m_\chi) M_n(m_\chi, Q_{\mathrm{thr}} = 0). \tag{45}$$

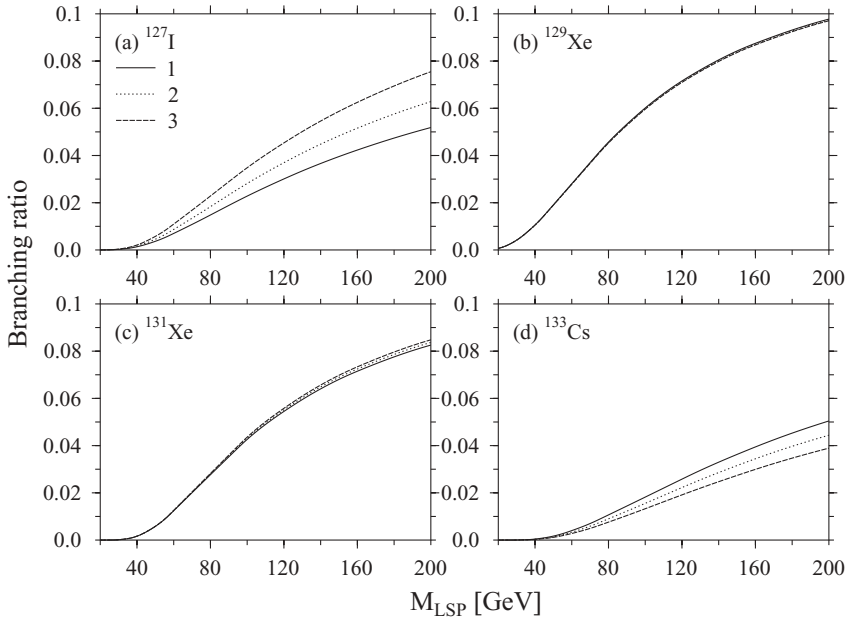


FIG. 15. The branching ratios [Eq. (40)] for $^{127}$I (a), $^{129}$Xe (b), $^{131}$Xe (c), and $^{133}$Cs (d). The threshold energy is $Q_{\mathrm{thr}} = 0$.

TABLE V. Computed auxiliary nuclear-structure coefficients $d_n(m_\chi)$ in units of $\mathrm{yr}^{-1}\ \mathrm{kg}^{-1}$ for elastic LSP-nucleus scattering off the discussed nuclei. The $d_n$ for any LSP mass $m_\chi$ can be linearly interpolated between the given values of $m_\chi$.

| | $m_\chi$ (GeV) | | | | | | $\alpha_n$ | $\beta_n$ |
|---|---|---|---|---|---|---|---|---|
| | 50 | 75 | 100 | 150 | 200 | 300 | | |
| $^{127}$I | | | | | | | | |
| $d_1$ | 52.2 | 43.8 | 37.0 | 27.9 | 22.3 | 15.9 | 0.0277 | 0.000111 |
| $d_2$ | 43.1 | 36.6 | 31.1 | 23.6 | 19.0 | 13.6 | 0.0279 | 0.000077 |
| $d_3$ | 35.8 | 30.8 | 26.6 | 20.4 | 16.5 | 11.9 | 0.0283 | 0.000030 |
| $d_4$ | 163.0 | 136.0 | 113.0 | 82.6 | 64.6 | 44.6 | 0.0198 | 0.000260 |
| $^{129}$Xe | | | | | | | | |
| $d_1$ | 100.8 | 83.0 | 69.0 | 50.9 | 40.2 | 28.3 | 0.0241 | 0.000226 |
| $-d_2$ | 101.6 | 83.7 | 69.5 | 51.2 | 40.5 | 28.5 | 0.0240 | 0.000229 |
| $d_3$ | 102.5 | 84.4 | 70.1 | 51.6 | 40.8 | 28.7 | 0.0239 | 0.000232 |
| $d_4$ | 160.5 | 133.7 | 111.0 | 81.0 | 63.2 | 43.7 | 0.0196 | 0.000267 |
| $^{131}$Xe | | | | | | | | |
| $d_1$ | 14.9 | 14.8 | 14.2 | 12.4 | 10.8 | 8.4 | 0.0302 | −0.000213 |
| $-d_2$ | 14.8 | 14.6 | 14.0 | 12.3 | 10.7 | 8.3 | 0.0302 | −0.000212 |
| $d_3$ | 14.7 | 14.5 | 13.9 | 12.2 | 10.6 | 8.2 | 0.0302 | −0.000212 |
| $d_4$ | 157.8 | 131.2 | 108.7 | 79.3 | 61.8 | 42.7 | 0.0195 | 0.000276 |
| $^{133}$Cs | | | | | | | | |
| $d_1$ | 19.3 | 17.2 | 15.4 | 12.6 | 10.6 | 8.1 | 0.0341 | −0.000141 |
| $d_2$ | 23.0 | 20.3 | 17.9 | 14.4 | 12.1 | 9.1 | 0.0338 | −0.000111 |
| $d_3$ | 27.5 | 23.9 | 20.9 | 16.6 | 13.8 | 10.3 | 0.0335 | −0.000078 |
| $d_4$ | 155.4 | 129.0 | 106.9 | 77.8 | 60.7 | 41.9 | 0.0193 | 0.000282 |

The redefined SUSY parameters are given by

$$f_1 \equiv \left(f_A^0\right)^2, \quad f_2 \equiv 2 f_A^0 f_A^1, \quad f_3 \equiv \left(f_A^1\right)^2, \\ f_4 \equiv A^2 \left(f_S^0 - f_S^1 \frac{A-2Z}{A}\right)^2. \tag{46}$$

We can average the $D_n$ coefficients over $a$ to produce their annual average values $\bar{D}_n$ in Eqs. (42) and (43). Let us denote by $d_n$ the $Q_{\mathrm{thr}} = 0$ values of $\bar{D}_n$ and so then the $d_n$ depend only on $m_\chi$. In Table V we list these $d_n$ coefficients for elastic LSP-nucleus scattering off all the discussed nuclei (in units of $\mathrm{yr}^{-1}\ \mathrm{kg}^{-1}$) for selected values of $m_\chi$. The $Q_{\mathrm{thr}}$ dependence of $\bar{D}_n$ can be conveniently fitted by the exponential

$$\bar{D}_n(m_\chi, Q_{\mathrm{thr}}) = e^{-(\alpha_n + \beta_n \mu_r) Q_{\mathrm{thr}}} d_n(m_\chi) \tag{47}$$

for $0 \leqslant Q_{\mathrm{thr}} \leqslant 30$ keV. Here the reduced mass $\mu_r$ of the nucleus-LSP system is given in units of GeV and $Q_{\mathrm{thr}}$ in units of keV. (The accuracy of this fit can be ascertained by studying Table IX.) Our parametrization [Eq. (47)] enables an easy extraction of $\bar{D}_n$ for the wanted LSP mass and detector threshold energy.

From Table V we notice that the coherent channel, represented by $d_4$ through Eq. (47), is strong. The importance of this channel is enhanced further by the fact that it is proportional to $A^2$, as seen from Eq. (3). From the table one sees also that for $^{129}$Xe the coherent channel is relatively weaker than for the other three mentioned nuclei.

TABLE VI. Computed annual averaged coefficients $\bar{E}_n(m_\chi)$, in units of $\mathrm{yr}^{-1}\ \mathrm{kg}^{-1}$, for inelastic LSP-nucleus scattering off the discussed nuclei. The values of $\bar{E}_n$ for any LSP mass $m_\chi$ can be linearly interpolated between the given values of $m_\chi$. The detector threshold is assumed to be zero.

| | $m_\chi$ (GeV) | | | | | |
|---|---|---|---|---|---|---|
| | 50 | 75 | 100 | 150 | 200 | 300 |
| $^{127}$I | | | | | | |
| $\bar{E}_1$ | 0.191 | 0.565 | 0.862 | 1.148 | 1.219 | 1.156 |
| $\bar{E}_2$ | 0.195 | 0.587 | 0.898 | 1.198 | 1.271 | 1.203 |
| $\bar{E}_3$ | 0.205 | 0.620 | 0.951 | 1.269 | 1.345 | 1.270 |
| $^{129}$Xe | | | | | | |
| $\bar{D}_1$ | 1.94 | 3.58 | 4.41 | 4.68 | 4.36 | 3.56 |
| $-\bar{D}_2$ | 1.95 | 3.60 | 4.42 | 4.70 | 4.37 | 3.57 |
| $\bar{D}_3$ | 1.96 | 3.61 | 4.44 | 4.72 | 4.39 | 3.58 |
| $^{131}$Xe | | | | | | |
| $\bar{D}_1$ | 0.086 | 0.359 | 0.625 | 0.904 | 0.970 | 0.905 |
| $-\bar{D}_2$ | 0.086 | 0.359 | 0.625 | 0.907 | 0.973 | 0.908 |
| $\bar{D}_3$ | 0.086 | 0.359 | 0.627 | 0.909 | 0.977 | 0.912 |
| $^{133}$Cs | | | | | | |
| $\bar{E}_1$ | 0.032 | 0.151 | 0.283 | 0.472 | 0.562 | 0.599 |
| $\bar{E}_2$ | 0.032 | 0.149 | 0.281 | 0.469 | 0.559 | 0.596 |
| $\bar{E}_3$ | 0.032 | 0.148 | 0.280 | 0.467 | 0.558 | 0.595 |

TABLE VII. Computed auxiliary annual modulation parameters $m_n(m_\chi)$ for elastic LSP-nucleus scattering. The $m_n$ for any LSP mass $m_\chi$ can be linearly interpolated between the given values of $m_\chi$. The annual modulation amplitudes are obtained from $m_n$ by the use of Eq. (48).

| | $M_{\rm LSP}$ (GeV) | | | | | | $\gamma_n$ | $\delta_n \times 10^5$ |
|---|---|---|---|---|---|---|---|---|
| | 50 | 75 | 100 | 150 | 200 | 300 | | |
| $^{127}$I | | | | | | | | |
| $m_1$ | 0.0012 | −0.0054 | −0.0089 | −0.0124 | −0.0143 | −0.0163 | 0.00119 | −0.51 |
| $m_2$ | 0.0022 | −0.0042 | −0.0076 | −0.0110 | −0.0129 | −0.0150 | 0.00120 | −0.54 |
| $m_3$ | 0.0037 | −0.0024 | −0.0056 | −0.0090 | −0.0109 | −0.0130 | 0.00123 | −0.59 |
| $m_4$ | 0.0023 | −0.0067 | −0.0120 | −0.0176 | −0.0204 | −0.0231 | 0.00129 | −1.03 |
| $^{129}$Xe | | | | | | | | |
| $m_1$ | −0.0001 | −0.0080 | −0.0122 | −0.0160 | −0.0176 | −0.0189 | 0.00105 | −0.35 |
| $m_2$ | −0.0001 | −0.0081 | −0.0123 | −0.0161 | −0.0177 | −0.0190 | 0.00105 | −0.36 |
| $m_3$ | −0.0001 | −0.0081 | −0.0124 | −0.0162 | −0.0178 | −0.0192 | 0.00106 | −0.37 |
| $m_4$ | 0.0020 | −0.0070 | −0.0124 | −0.0179 | −0.0207 | −0.0234 | 0.00128 | −1.01 |
| $^{131}$Xe | | | | | | | | |
| $m_1$ | 0.0144 | 0.0140 | 0.0130 | 0.0100 | 0.0072 | 0.0035 | 0.00152 | −1.21 |
| $m_2$ | 0.0143 | 0.0138 | 0.0129 | 0.0099 | 0.0071 | 0.0034 | 0.00152 | −1.21 |
| $m_3$ | 0.0143 | 0.0137 | 0.0127 | 0.0098 | 0.0070 | 0.0034 | 0.00152 | −1.20 |
| $m_4$ | 0.0016 | −0.0074 | −0.0128 | −0.0183 | −0.0210 | −0.0237 | 0.00127 | −1.00 |
| $^{133}$Cs | | | | | | | | |
| $m_1$ | 0.0052 | 0.0021 | 0.0010 | 0.0000 | −0.0004 | −0.0007 | 0.00130 | −0.57 |
| $m_2$ | 0.0041 | 0.0004 | −0.0010 | −0.0023 | −0.0028 | −0.0032 | 0.00126 | −0.49 |
| $m_3$ | 0.0030 | −0.0011 | −0.0028 | −0.0044 | −0.0050 | −0.0054 | 0.00123 | −0.42 |
| $m_4$ | 0.0014 | −0.0078 | −0.0131 | −0.0186 | −0.0213 | −0.0240 | 0.00126 | −0.98 |

In Table VI we present the computed annual-averaged coefficients $\bar{E}_n(m_\chi)$ of Eqs. (44) and (45) for inelastic LSP-nucleus scattering off the discussed nuclei. As usual, we have assumed that the detector threshold is zero. Comparing Tables V and VI one notices that overall the $\bar{E}_n$ coefficients are much smaller than the $d_n = \bar{D}_n(Q_{\rm thr} = 0)$ coefficients of elastic scattering. The ratio of $d_n$ and $\bar{E}_n$, for $n = 1, 2, 3$, ranges from some 10 to some 200, being smaller for larger LSP masses. These considerations, and the fact that the spin-independent channel is missing from the inelastic scattering, tell us that the inelastic channel is quite suppressed relative to the elastic channel.

To access the annual modulation $M_n(m_\chi, Q_{\rm thr})$ of the $D_n$ coefficients we perform the following parametrization. Like the annual average values, the coefficients $M_n$ can be fitted as functions of the detector threshold by

$$M_n(m_\chi, Q_{\rm thr}) = m_n(m_\chi) + (\gamma_n + \delta_n \mu_r) Q_{\rm thr}, \qquad (48)$$

where $\mu_r$ is the reduced mass in GeV and $Q_{\rm thr}$ is inserted in units of keV. (The accuracy of this fit can be ascertained by studying Table IX.) The quantities $m_n(m_\chi)$ have been tabulated in Table VII for all the nuclei of interest in this work. The same has been done for the quantities $M_n(m_\chi, Q_{\rm thr} = 0)$ of Eq. (45) in Table VIII. Here it is worth pointing out that for the target nuclei of Table VII the modulation amplitude $M_n$ of Eq. (48) can become negative for heavy LSPs, leading to a negative modulation (i.e., the oscillation maximum is then predicted to be on December 2 instead of June 2).

To test the accuracy of the fits given by Eqs. (47) and (48) we have chosen some values of the LSP mass $m_\chi$ and threshold

TABLE VIII. Computed annual modulation factors $M_n(m_\chi, Q_{\rm thr} = 0)$ for inelastic LSP-nucleus scattering. The $M_n$ for any LSP mass $m_\chi$ can be linearly interpolated between the given values of $m_\chi$.

| | $M_{\rm LSP}$ (GeV) | | | | | |
|---|---|---|---|---|---|---|
| | 50 | 75 | 100 | 150 | 200 | 300 |
| $^{127}$I | | | | | | |
| $M_1$ | 0.189 | 0.146 | 0.124 | 0.103 | 0.093 | 0.082 |
| $M_2$ | 0.189 | 0.146 | 0.124 | 0.103 | 0.092 | 0.081 |
| $M_3$ | 0.190 | 0.147 | 0.124 | 0.103 | 0.092 | 0.081 |
| $^{129}$Xe | | | | | | |
| $M_1$ | 0.137 | 0.106 | 0.088 | 0.068 | 0.058 | 0.047 |
| $M_2$ | 0.137 | 0.106 | 0.088 | 0.068 | 0.058 | 0.047 |
| $M_3$ | 0.137 | 0.106 | 0.088 | 0.068 | 0.058 | 0.047 |
| $^{131}$Xe | | | | | | |
| $M_1$ | 0.246 | 0.186 | 0.158 | 0.129 | 0.115 | 0.100 |
| $M_2$ | 0.246 | 0.186 | 0.158 | 0.129 | 0.115 | 0.100 |
| $M_3$ | 0.247 | 0.186 | 0.158 | 0.129 | 0.115 | 0.100 |
| $^{133}$Cs | | | | | | |
| $M_1$ | 0.250 | 0.189 | 0.163 | 0.137 | 0.124 | 0.110 |
| $M_2$ | 0.250 | 0.189 | 0.163 | 0.137 | 0.124 | 0.110 |
| $M_3$ | 0.250 | 0.189 | 0.163 | 0.137 | 0.124 | 0.110 |

TABLE IX. Comparison between the fits of Eqs. (47) and (48) and the corresponding calculated coefficients.

| Coefficient | $\bar{D}_1$ | | $\bar{D}_4$ | | $M_1$ | | $M_4$ | |
|---|---|---|---|---|---|---|---|---|
| $m_\chi$ | 100 GeV | | 300 GeV | | 100 GeV | | 300 GeV | |
| $Q_{\rm thr}$ (keV) | fit | calc. | fit | calc. | fit | calc. | fit | calc. |
| 10.0 | 26.4 | 26.3 | 29.3 | 29.0 | 0.0002 | −0.0002 | −0.0190 | −0.0184 |
| 20.0 | 18.8 | 18.9 | 19.3 | 18.5 | 0.0094 | 0.0086 | −0.0149 | −0.0139 |
| 30.0 | 13.4 | 13.7 | 12.7 | 11.6 | 0.0185 | 0.0172 | −0.0108 | −0.0093 |

energy $Q_{\rm thr}$ to compare the fitted values and calculated values of some $\bar{D}_n$ and $M_n$ coefficients. This comparison is performed in Table IX. As can be seen the accuracy of the fit decreases when going to higher values of the threshold energy. The value $Q_{\rm thr} = 30$ keV begins already to be at the limits of a level of reasonable accuracy. For $M_1$ at $Q_{\rm thr} = 10$ keV the computed value happens to be close to zero and negative whereas the fit gives a small positive value. The relative difference is thus large but the absolute difference is small. The same situation is seen in all cases where the modulation amplitudes $M_n$ go through zero and change sign. For the application of the fitted values, passing the zero point is no problem since both the fit and the calculation give the same answer: a practically zero modulation.

One can test the previously described formalism for elastic and inelastic LSP-nucleus scattering by choosing a subset of SUSY parametrizations [Eq. (46)] proposed as models A, B, and C in Refs. [25,40]. There values were assigned to the isoscalar ($f_A^0$) and isovector ($f_A^1$) axial-current parameters and the isoscalar ($f_S^0$) and isovector ($f_S^1$) scalar-current parameters. In Refs. [25,40] the authors discuss difficulties in assigning values to these parameters and they base their choice of parameter values on the numerical fits of the basic SUSY parameters in Ref. [44]. In this way a representative sample of three different solutions (S1, S2, and S3) was chosen.

According to our calculations the most favorable detection rates for elastic scattering stem from the SUSY models where the spin-independent coherent contribution is dominant. In this case for many of the SUSY models listed here the detection rates are more than a hundred events/yr/kg for all the discussed nuclei. Such large detection rates have already been excluded by the present WIMP detection experiments. Combining the present experimental data [7,12,13] with our computed nuclear response suggests that practically all of the SUSY scenarios of [25,40] are ruled out. For the inelastic channel the highest detection rates turn out to be of the order of $10^{-3}$ events/yr/kg. This is still some two orders of magnitude beyond the sensitivity of the DAMA/WIMP-$^{129}$Xe experiment [10].

## VI. CONCLUSIONS

In this article we have discussed detection rates for elastic and inelastic LSP-nucleus scattering on $^{127}$I, $^{129}$Xe, $^{131}$Xe, and $^{133}$Cs. The corresponding nuclear-structure calculations were done by using the nuclear shell model in a model space involving the $0g_{7/2}, 1d_{5/2}, 2s_{1/2}, 1d_{3/2}$, and $0h_{11/2}$ single-particle orbitals and using realistic nucleon-nucleon forces derived from the Bonn-CD $G$ matrix. Both the elastic and inelastic channels have been described within the same unified microscopic nuclear scheme. The relevant experimental observables, including magnetic moments of the involved nuclear states, as well as $M1$ transitions between them, are reproduced quite well by fitted nuclear gyromagnetic factors.

We presented a useful parametrization of the elastic detection rates in terms of the LSP mass and detector threshold energy. The inelastic rates have been calculated by assuming zero threshold. The obtained results are of interest, for example, for the DAMA ($^{127}$I and $^{129}$Xe), KIMS ($^{127}$I and $^{133}$Cs), NAIAD and COUPP ($^{127}$I), and ZEPLIN, XENON, and XMASS ($^{129}$Xe and $^{131}$Xe) experimental programs.

## ACKNOWLEDGMENTS

The authors thank Profs. J. D. Vergados and T. H. Kosmas for useful discussions about the inelastic channel of the LSP-nucleus scattering. This work has been partially supported by the Academy of Finland under the Finnish Centre of Excellence Programme 2006–2011 (Nuclear and Accelerator Based Programme at JYFL). We thank also the EU ILIAS project under Contract No. RII3-CT-2004-506222.

[1] G. Jungman, M. Kamionkowski, and K. Griest, Phys. Rep. **267**, 195 (1996).
[2] S. T. Lin *et al.*, arXiv:0712.1645 [hep-ex].
[3] D. S. Akerib *et al.*, Phys. Rev. Lett. **96**, 011302 (2006); D. S. Akerib *et al.*, Phys. Rev. D **73**, 011102 (2006).
[4] V. Sanglard *et al.*, Phys. Rev. D **71**, 122002 (2005).
[5] G. Angloher *et al.*, Astropart. Phys. **23**, 325 (2005).
[6] G. J. Alner *et al.*, Astropart. Phys. **23**, 444 (2005).
[7] J. Angle *et al.*, Phys. Rev. Lett. **100**, 021303 (2008).
[8] P. Belli *et al.*, Phys. Lett. **B387**, 222 (1996).
[9] R. Bernabei *et al.*, Phys. Lett. **B436**, 379 (1998).
[10] R. Bernabei *et al.*, New J. Phys. **2**, 15 (2000).
[11] K. Ueshima *et al.*, Nucl. Inst. Meth. A **594**, 148 (2008).
[12] H. S. Lee *et al.*, Phys. Rev. Lett. **99**, 091301 (2007).
[13] N. J. C. Spooner *et al.*, Phys. Lett. **B473**, 330 (2000).
[14] S. Cebrián *et al.*, Astropart. Phys. **15**, 79 (2001).
[15] T. A. Girard *et al.*, Phys. Lett. **B621**, 233 (2005).
[16] M. Barnabe-Heider *et al.*, Phys. Lett. **B624**, 186 (2005).
[17] E. Behnke *et al.*, Science **319**, 933 (2008).

[18] R. Bernabei *et al.*, Phys. Lett. **B424**, 195 (1998); R. Bernabei *et al.*, *ibid.* **B450**, 448 (1999).
[19] R. Bernabei *et al.*, Phys. Lett. **B480**, 23 (2000); R. Abusaidi *et al.*, Phys. Rev. Lett. **84**, 5699 (2000).
[20] R. Bernabei *et al.*, Riv. Nuovo Cimento **26**, 1 (2003).
[21] M. Kortelainen, T. S. Kosmas, J. Suhonen, and J. Toivanen, Phys. Lett. **B632**, 226 (2006).
[22] J. D. Vergados, Phys. Rev. Lett. **83**, 3597 (1999); Phys. Rev. D **62**, 023519 (2000); **67**, 103003 (2003).
[23] M. E. Gomez and J. D. Vergados, Phys. Lett. **B512**, 252 (2001); M. E. Gomez, G. Lazarides, and C. Pallis, *ibid.* **B487**, 313 (2000); Phys. Rev. D **61**, 123512 (2000).
[24] J. D. Vergados and H. Ejiri, Phys. Lett. **B606**, 313 (2005).
[25] T. S. Kosmas and J. D. Vergados, Phys. Rev. D **55**, 1752 (1997); J. D. Vergados and T. S. Kosmas, Phys. At. Nucl. **61**, 1066 (1998).
[26] P. Toivanen, M. Kortelainen, J. Suhonen, and J. Toivanen, Phys. Lett. **B666**, 1 (2008).
[27] A. K. Drukier, K. Freese, and D. N. Spergel, Phys. Rev. D **33**, 3495 (1986); J. Ellis and R. A. Flores, Nucl. Phys. **B307**, 883 (1988).
[28] J. Engel and P. Vogel, Phys. Rev. D **40**, 3132 (1989).
[29] J. Engel, Phys. Lett. **B264**, 114 (1991).
[30] F. Iachello, L. M. Krauss, and G. Maino, Phys. Lett. **B254**, 220 (1991).
[31] M. A. Nikolaev and H. V. Klapdor-Kleingrothaus, Z. Phys. A **345**, 373 (1993).
[32] M. T. Ressell and D. J. Dean, Phys. Rev. C **56**, 535 (1997).
[33] E. Holmlund, M. Kortelainen, T. S. Kosmas, J. Suhonen, and J. Toivanen, Phys. Lett. **B584**, 31 (2004).
[34] J. D. Vergados, P. Quentin, and D. Strottman, Int. J. Mod. Phys. E **14**, 751 (2005).
[35] J. Ellis, R. A. Flores, and J. D. Lewin, Phys. Lett. **B212**, 375 (1988).
[36] J. Engel and P. Vogel, Phys. Rev. D **61**, 063503 (2000).
[37] J. Toivanen, computer code EICODE, JYFL, Finland, 2004.
[38] M. Hjorth-Jensen, T. T. S. Kuo, and E. Osnes, Phys. Rep. **260**, 125 (1995); M. Hjorth-Jensen (private communication).
[39] M. Horoi, B. A. Brown, and V. Zelevinsky, Phys. Rev. C **50**, R2274 (1994).
[40] J. D. Vergados, J. Phys. G: Nucl. Part. Phys. **22**, 253 (1996).
[41] J. Suhonen, *From Nucleons to Nucleus: Concepts of Microscopic Nuclear Theory* (Springer-Verlag, Berlin, 2007).
[42] R. Helm, Phys. Rev. **104**, 1466 (1956).
[43] G. Duda, A. Kemper, and P. Gondolo, J. Cosmol. Astropart. Phys. 04 (2007) 012.
[44] G. L. Kane, C. Kolda, L. Roszkowski, and J. D. Wells, Phys. Rev. D **49**, 6173 (1994).